Climate Dynamics

West African monsoon decadal variability and surface-related forcings: Second West African Monsoon Modeling and Evaluation Project Experiment (WAMME II)
--Manuscript Draft--

Manuscript Number:	CLDY-D-15-00403R3
Full Title:	West African monsoon decadal variability and surface-related forcings: Second West African Monsoon Modeling and Evaluation Project Experiment (WAMME II)
Article Type:	S.I. : Decadal variability of West African monsoon
Keywords:	Sahel seasonal and decadal climate variability; Sahel drought, SST and land forcings; GCM
Corresponding Author:	Yongkang Xue University of California Los Angeles LA, UNITED STATES
Corresponding Author Secondary Information:	
Corresponding Author's Institution:	University of California Los Angeles
Corresponding Author's Secondary Institution:	
First Author:	Yongkang Xue
First Author Secondary Information:	
Order of Authors:	Yongkang Xue
	Fernando De Sales
	William K-M Lau
	Aaron Boone
	Kyu-Myong Kim
	Carlos R Mechoso
	Guiling Wang
	Fred Kucharski
	Kathleen Schiro
	Masahiro Hosaka
	Suosuo Li
	Leonard M Druyan
	Ibrah Seidou Sanda
	Wassila Thiaw
	Ning Zeng
	Ruth E Comer
	Young-Kwon Lim
	Sarith Mahanama
	Guoqiong Song
	Yu Gu
	Samson M Hagos
	Mian Chin

	Siegfried Schubert
	Paul Dirmeyer
	L Ruby Leung
	Eugenia Kalnay
	Akio Kitoh
	Cheng-Hsuan Lu
	Natalie M Mahowald
	Zhengqiu Zhang
Order of Authors Secondary Information:	
Funding Information:	National Science Foundation (US) (AGS-1115506)	Dr. Yongkang Xue
	National Science Foundation (US) (AGS-1419526)	Dr. Yongkang Xue

Abstract:

The second West African Monsoon Modeling and Evaluation Project Experiment (WAMME II) is designed to improve understanding of the possible roles and feedbacks of sea surface temperature (SST), land use land cover change (LULCC), and aerosols forcings in the Sahel climate system at seasonal to decadal scales. The project's strategy is to apply prescribed observationally based anomaly forcing, i.e., "idealized but realistic" forcing, in simulations by climate models. The goal is to assess these forcings' effects in producing/amplifying seasonal and decadal climate variability in the Sahel between the 1950s and the 1980s, which is selected to characterize the great drought period of the last century.   This is the first multi-model experiment specifically designed to simultaneously evaluate such relative contributions.

The WAMME II models have consistently demonstrated that SST forcing is a major contributor to the 20th century Sahel drought. Under the influence of the maximum possible SST forcing, the ensemble mean of WAMME II models can produce up to 60% of the precipitation difference during the period. The present paper also addresses the role of SSTs in triggering and maintaining the Sahel drought. In this regard, the consensus of WAMME II models is that both Indian and Pacific Ocean SSTs greatly contributed to the drought, with the former producing an anomalous displacement of the Intertropical Convergence Zone (ITCZ) before the WAM onset, and the latter mainly contributes to the summer WAM drought.

The WAMME II models also show that the impact of LULCC forcing on the Sahel climate system is weaker than that of SST forcing, but still of first order magnitude. According to the results, under LULCC forcing the ensemble mean of WAMME II models can produces about 40% of the precipitation difference between the 1980s and the 1950s. The role of land surface processes in responding to and amplifying the drought is also identified. The results suggest that catastrophic consequences are likely to occur in the regional Sahel climate when SST anomalies in individual ocean basins and in land conditions combine synergistically to favor drought.

1   West African monsoon decadal variability and surface-related forcings:

2   Second West African Monsoon Modeling and Evaluation Project

3   Experiment (WAMME II)

4

5   Yongkang Xue[1], Fernando De Sales[2], William K-M Lau[3], Aaron Boone[4], Kyu-Myong Kim[5],

6   Carlos R. Mechoso[1], Guiling Wang[6], Fred Kucharski[7], Kathleen Schiro[1], Masahiro Hosaka[8],

7   Suosuo Li[9,1], Leonard M. Druyan[10], Ibrah Seidou Sanda[11], Wassila Thiaw[12], Ning Zeng[3], Ruth E.

8   Comer[13], Young-Kwon Lim[5,14], Sarith Mahanama[5], Guoqiong Song[1], Yu Gu[1], Samson M Hagos[16],

9   Mian Chin[5], Siegfried Schubert[5], Paul Dirmeyer[15], L. Ruby Leung[16], Eugenia Kalnay[3], Akio

10   Kitoh[17], Cheng-Hsuan Lu[12,18], Natalie M. Mahowald[19], Zhengqiu Zhang[20,1]

11

12   1). University of California, Los Angeles, CA, USA
13   2). San Diego State University, CA, USA
14   3). University of Maryland, College Park, MD, USA
15   4). Centre National de Recherches Météorologiques, Météo-France, Toulouse, France
16   5). NASA Goddard Space Flight Center, Greenbelt, MD, USA
17   6). University of Connecticut, Storrs, CT, USA
18   7). The International Center for Theoretical Physics, Trieste, Italy
19   8). Meteorological Research Institute, Tsukuba, Japan
20   9). Cold and Arid Regions Environmental and Engineering Research Institute, Chinese Academy
21   of Sciences, Lanzhou, China
22   10). NASA Goddard Institute for Space Studies and Columbia University, New York, NY, USA
23   11). AGRHYMET Regional Center and Abdou Moumouni University, Niamey, Niger
24   12). National Center for Environmental Prediction, College Park, MD, USA
25   13). Met Office Hadley Centre, Exeter, U.K.
26   14). Goddard Earth Sciences Technology and Research, I. M. Systems Group, MD, USA
27   15). Center for Ocean-Land-Atmosphere Interactions Studies, George Mason University,
28   Fairfax, VA, USA
29   16). Pacific Northwest National Laboratory. Richland, WA, USA
30   17). University of Tsukuba, Tsukuba, Japan
31   18). University at Albany, State University of New York, NY, USA
32   19). Cornell University, Ithaca, NY, USA
33   20). Chinese Academy of Meteorological Sciences, Beijing, China

34

35   May 2016

36

37   Submission to Climate Dynamics Special Issue

Abstract

The second West African Monsoon Modeling and Evaluation Project Experiment (WAMME II) is designed to improve understanding of the possible roles and feedbacks of sea surface temperature (SST), land use land cover change (LULCC), and aerosols forcings in the Sahel climate system at seasonal to decadal scales. The project's strategy is to apply prescribed observationally based anomaly forcing, i.e., "idealized but realistic" forcing, in simulations by climate models. The goal is to assess these forcings' effects in producing/amplifying seasonal and decadal climate variability in the Sahel between the 1950s and the 1980s, which is selected to characterize the great drought period of the last century.   This is the first multi-model experiment specifically designed to simultaneously evaluate such relative contributions.

The WAMME II models have consistently demonstrated that SST forcing is a major contributor to the 20th century Sahel drought. Under the influence of the maximum possible SST forcing, the ensemble mean of WAMME II models can produce up to 60% of the precipitation difference during the period. The present paper also addresses the role of SSTs in triggering and maintaining the Sahel drought. In this regard, the consensus of WAMME II models is that both Indian and Pacific Ocean SSTs greatly contributed to the drought, with the former producing an anomalous displacement of the Intertropical Convergence Zone (ITCZ) before the WAM onset, and the latter mainly contributes to the summer WAM drought.

The WAMME II models also show that the impact of LULCC forcing on the Sahel climate system is weaker than that of SST forcing, but still of first order magnitude.   According to the results, under LULCC forcing the ensemble mean of WAMME II models can produces about 40% of the precipitation difference between the 1980s and the 1950s. The role of land surface processes in responding to and amplifying the drought is also identified. The results suggest that catastrophic

61   consequences are likely to occur in the regional Sahel climate when SST anomalies in individual

62   ocean basins and in land conditions combine synergistically to favor drought.

63   .

64   **Key Words: Sahel seasonal and decadal climate variability; Sahel drought, SST and land**

65   **forcings; GCM**

1). Introduction

The Sahel is a climatically diverse and economically fragile region. The dramatic changes that occurred over Sahelian Africa from wet conditions in the 1950s to much drier conditions in the 1970s-1980s to be followed by partial recovery after the 1980s represent one of the strongest inter-decadal climate variabilities and the longest drought on the planet in the twentieth century (e.g., Redelsperger et al. 2007; Lebel and Ali, 2009; Nicholson et al., 2012). A significant climate feature in Sahelian Africa is the West African monsoon (WAM), which exerts a strong control on climate variability in the Sahel. Observational evidence has supported the notion that there is strong decadal climate variability in the Sahel and surrounding areas from the 1950s to the 2000s, not only in precipitation, but also in vegetation conditions, land use and land cover (LULC) change, and aerosol loading.

Numerous papers have discussed SST variability in the last century and its links to Sahelian precipitation variability. Relationships between Sahel precipitation and SST anomalies in the Atlantic, Pacific, and Indian Oceans and the Mediterranean Sea[1] have been studied extensively (see a comprehensive review in Rodríguez-Fonseca et al., 2015). Despite the dominant role of SST anomalies on Sahel climate variability, modeling studies have consistently shown that SST is not the sole forcing of significant Sahel climate variability and other sources of forcing should be considered.

Although a number of atmospheric general circulation models (AGCMs) are able to reproduce the 20th century drying trend in West Africa and the Sahel dry conditions of the 1970-80s and subsequent rainfall recovery using the observed SST as boundary conditions, simulated trends and drying are substantially weaker than in the observations (e.g., Giannini et al., 2003; Lu

---

[1] For convenience, when we use the word "oceans" in this paper the Mediterranean Sea will be included.

88   and Delworth, 2005; Hoerling et al. 2006, 2010; Lau et al., 2006; Caminade and Terray, 2010;

89   Martin and Chorncroft, 2014). For instance, the Climate of the 20th Century international project

90   (C20C, Scaife et al., 2009) used 14 state-of-the-art GCMs with observed SSTs and other relevant

91   data to study climate variations and changes over the last century. Only two C20C models

92   simulated about half the magnitude of the Sahel rainfall changes between the 1950s and the 1980s.

93   The results of the other models ranged between less than 30% of the observed precipitation

94   anomaly to even no negative anomalies at all. Scaife et al. (2009) concluded that the Sahel drought

95   was only partly forced by SSTs in their experiment, which did not reproduce the magnitude of the

96   Sahel drought. In spite of previous efforts to evaluate the SST contribution, a number of important

97   questions remain unanswered. For instance, do different ocean basins provide a similar

98   contribution to Sahelian precipitation variability or are some basins more influential than others?

99   Rodríguez-Fonseca et al. (2015) pointed out that aspects on these questions remain open. The

100   results obtained so far appear to be highly model dependent (e.g. Scaife et al., 2009; Biasutti et al.,

101   2008). The possible nonlinearities in the atmospheric response to different SST anomalies and

102   interactions among the basins complicate the problem (Hagos and Cook, 2008).

103   In addition to SST effect, the Sahel has been identified as the region in the world where

104   climate is most sensitive to land/atmosphere interactions through vegetation and soil processes

105   (e.g., Koster et al., 2004; Xue et al., 2004b, 2010a; see also reviews in Xue et al., 2004a, 2012).

106   The C20C experiment also noted that the two models that captured the large change in Sahel

107   rainfall include land surface effects via either parameterized vegetation-climate interactions or

108   specified land use and land cover changes (LULCC). The present study evaluates and compares

109   the effects of both SST and land surface processes (mainly through LULCC experiments) on the

110   Sahel decadal variability in precipitation, surface temperature, atmospheric circulation, and surface

111   energy balance, especially during the drought of the 1980s. This comparison has not been

112   conducted before. The Sahel decadal precipitation anomalies between the 1980s and the 1950s

113   are used to characterize the Sahel 1980s drought in this study.

114   While a careful comparison of the contributions of SST, land, and other forcings to the

115   Sahel drought is imperative to unravel the root causes of the long-term variations of the Sahel

116   climate, it has not been performed in multi-modeling contexts. Our approach is based on the

117   examination of the results from the West African Monsoon Modeling and Evaluation Project

118   Experiment II (WAMME II). Since it is challenging to simulate the spatial dimensions, temporal

119   evolution, triggering and strength of the West African Monsoon (WAM) system (e.g., Hourdin et

120   al., 2010; Roehrig et al., 2013), in the first WAMME experiment (WAMME I), we

121   comprehensively evaluated the performances of WAMME GCMs and RCMs in simulating the

122   variability of West African monsoon (WAM) precipitation, surface temperature, and major

123   circulation features at seasonal and intraseasonal scales (Xue et al., 2010; Druyan et al., 2010;

124   Boone et al., 2010). The results indicated that, despite deficiencies in many aspects, the WAMME

125   models generally produce reasonable simulations of the spatial distribution of WAM seasonal

126   mean precipitation and surface temperature and their temporal evolution, as well as some major

127   circulation features (Xue et al., 2010). The results from the WAMME I experiment provide a solid

128   foundation for us to work further in the WAMME II experiment.

129   In this study, we examine whether the reported influence by the global SST and by

130   individual Oceans' SST on the Sahel climate is simply an artifact of sampling variability or

131   whether such an influence reflects genuine and interesting long-term changes in the climate

132   system. The differences in seasonal WAM features at different decades are also evaluated.

133   Another issue addressed is whether the drought was primarily due to natural multi-decadal modes

134 of variability in the SST patterns or the results of anthropogenic effects. The objectives in this

135 WAMME II paper are to provide a basic understanding of the issues related to SST; and to assess

136 the relative contributions of forcings in SST and land surface processes in producing/amplifying

137 Sahelian seasonal and decadal climate variability. In the following text, section 2 introduces the

138 GCMs and the design of the WAMME II experiment. Section 3 evaluates the impact of SST

139 anomalies in the world ocean and individual ocean basins on Sahel climate variability, including

140 precipitation, surface temperature, surface energy balances, and some major circulation features.

141 The SST and LULCC effects are also compared. Section 4 summarizes results and discusses key

142 issues for future studies.

143 **2). WAMME Models and WAMME II Experimental Design**

144   The WAMME II project comprises 8 GCMs (Table 1a) and 4 RCMs (Table 1b) with a

145 wide range of spatial resolutions and physical parameterizations. Among the GCMs, the JMA

146 MRI (Japan Meteorological Administration Meteorological Research Institute, Mizuta et al., 2006)

147 GCM has the highest horizontal resolution (20 km) while the ICTP-UMD (International Center

148 for Theoretical Physics/University of Maryland, College Park; Kucharski et al., 2013) and the

149 UCLA AGCM (University of California, Los Angeles, Mechoso et al., 2000) have the lowest

150 resolutions (~200km). The UCONN CAM5 (University of Connecticut/Community Earth System

151 Model version 5. Neale et al., 2012) and GSFC GEOS-5 (the version 5 of the Goddard Earth

152 Observing System Model of the Global Modeling and Assimilation Office at NASA/GSFC. Molod

153 et al., 2012) include comprehensive aerosol schemes. All models include comprehensive

154 biophysical models for land surface processes. The UCLA GFS (Kanamitsu et al., 2002b; Xue et

155 al., 2004b) and the UCLA AGCM have the same land surface scheme. More information on the

156 physical components of participating models, including land surface models, can be found in Table

1. Among eight GCMs, the HadGEM2-A GCM (Pope et al., 2000) only participated in testing the LULCC effect. Two versions of the GSFC GEOS-5 have participated in the WAMME II experiments. In the SST experiments, the GSFC model includes the GOCART aerosol model (NASA Goddard Chemistry Aerosol Radiation and Transport, Chin et al., 2000, 2002). The GEOS-5 provides two sets of results with different aerosol optical properties (Referred to as GEOS-5 I and GEOS-5 II in this paper). In the GEOS-5 LULCC experiment, a catchment model is used with the land surface scheme (Koster et al., 2000). Except for the ICTP-UMD GCM, other WAMME II models have been validated in the WAMME I for their ability in simulating WAM precipitation and circulation (Xue et al., 2010a). The WAMME II models' ability to model the West African climatology is outlined in the electronic supplement of this paper. The WAMME II also includes regional climate models (Table 1b). Results from RCM in relation to monsoon response to LULCC and biomass burning are presented in separate papers (Hagos et al., 2014; De Sales et al., 2015; Wang et al., 2015).

The WAMME II control simulation (referred to as Case CTL) uses January 1, 2006, as the initial condition and time-varying climatological SSTs as boundary conditions. The models were integrated for 6 years and results that will be presented correspond to the average of the last five years. Since climatological SST is used and the first year's results are discarded, the effects of initial conditions are minimized. The ITCP-UMD GCM has a dynamic vegetation model that requires a 50-year model spin up; results presented here correspond to the last 50 years of simulation. By using the equilibrium type test, models should have less internal variability and produce clearer signals, which will facilitate understanding of the relevant mechanisms. The initial conditions for the atmosphere in the WAMME II experiment are from the NCEP/DOE (National Center for Environmental Prediction/Department of Energy) Reanalysis II (Kanamitsu et al.,

180   2002a). This Reanalysis version includes corrections of human processing errors and incorporates

181   upgrades to the forecast model and a diagnostic package that had been developed since the time

182   the Reanalysis I was finalized.

183   To test the impacts of SST and land forcings, the WAMME II strategy is to apply

184   observational data-based prescribed anomaly forcing, i.e., "idealized but realistic" forcing, in

185   GCM and RCM simulations. To analyze the effect of SST anomalies on Sahel precipitation, long-

186   term variations of global SST associated with the decadal dry and wet spells of Sahel rainfall are

187   reconstructed using SVD analysis. Annual cycles are removed based on 60-year monthly averages

188   for 1950-2009. To minimize the effect of interannual variation of SST, the ENSO signal is

189   removed based on linear regression between SST anomalies at each grid and the NINO3.4 SST

190   anomaly index. Possible residuals associated with the ENSO signal as well as shorter timescale

191   variations are further reduced by applying a 13-month moving average. SVD is then applied to

192   ENSO-free global SST and Sahel rainfall anomalies.

193   Figures 1a and1b show the first singular value decomposition mode (SVD1) for global SST

194   and WAM rainfall respectively, while Figure 1c display the times series of the first principal

195   components (PC1s). SVD analysis depicts the common patterns between two variables (Wallace

196   et al., 1992; Weng et al., 1999). SST and rainfall data used in the figure are from the Hadley Centre

197   Sea Ice and Sea Surface Temperature data set (Rayner et al. 2003) and the Climate Prediction

198   Center's global gauge-based analysis of precipitation (CPC GTS, Chen et al., 2002), respectively.

199   The leading SVD mode, which explains a significant covariance (67.2%) between SST and

200   rainfall, captures the well-known patterns of inter-decadal variation of SST and associated change

201   in rainfall over the Sahel. The inter-hemispheric asymmetry of SST anomalies in the Atlantic

202   Ocean and associated SST trends in the Indian Ocean and the Mediterranean Sea as displayed in

203 Figures 1a and 1c are consistent with results of previous studies (e.g. Lamb, 1978; Folland et al.

204 1991, Carton et al., 1996; Janicot et al., 1998; Rowell, 2001; Jolly et al., 2007; and Hastenrath and

205 Pozin 2010). The second SST mode (8.7%) shows a globally homogeneous spatial pattern

206 associated with rainfall change in the southern Sahel (5°N-12°N) and the PC2 has a weak trend

207 only after the mid-1970s. The third SST mode only explains 4.5% variance. The second and third

208 SVDs are not considered in our construction of the SST forcing as discussed below.

209 In WAMME II, the amplitude of the SST forcing field is required to be both realistic and

210 strong enough to achieve a robust model response, and to be consistent with that used in other

211 sensitivity experiments (e.g., LULCC and aerosol). To emphasize the effect of decadal SST

212 change on the Sahel rainfall between the 1950s and 1980s, the maximum value in the time series

213 of PC1 in the 1950s and the minimum value in the 1980s are used to reconstruct the SST anomalies

214 for those decades. This design is consistent with the "idealized but realistic" strategy of WAMME

215 II. Figure 1d shows the difference between reconstructed SST anomalies for the 1980s and 1950s.

216 The distribution and amplitude of SST anomalies are both comparable to those in previous studies

217 (e.g., Lu and Delworth, 2005; Mohino et al., 2011). These anomalies are added to the 60-year

218 monthly averages of 1950–2009 to construct an annual cycle of SST for the 1950s and the 1980s.

219 Since the primary interest is on decadal variability, constant SST anomalies in time are

220 superimposed on the SST seasonal cycle. In WAMME II, model runs similar to Case CTL but

221 with the prescribed SST anomalies for the 1950s and the 1980s are referred to as Case 50SST and

222 Case 80SST, respectively. In these two runs, except for the SST conditions, other initial

223 atmospheric and boundary conditions are the same as in Case CTL. The model results are bi-

224 linearly interpolated to the 0.5º CPC GTS (Chen et al., 2002) grid for comparison. We use

225   Reanalysis I for comparisons with simulation in the following text because only this reanalysis

226   dataset dates backs to the 1950s.

227   The WAMME II also investigates the impact of SST anomalies in different ocean basins.

228   The SST effect from one ocean basin over the Sahel could be direct (i.e., via teleconnections) or

229   indirect (i.e., through interaction with atmospheric anomalies caused by SST anomalies in other

230   ocean basins; then this interaction affects the Sahel climate variability via teleconnections) (e.g.,

231   Hagos and Cook, 2008). If we simply added one ocean's anomaly, this indirect effect may be

232   missing (because other ocean's anomalies are not imposed). Our approach was specifically

233   designed to accounts for both direct and indirect effects of each ocean's SST anomalies. The

234   approach we use in WAMME II consists of starting with the global 1950 SST anomalies and the

235   global 1980 SST anomalies in the cases that we will refer to as Case 50SST and Case 80SST,

236   respectively, which preserves the influence due to interactions of atmospheric circulation caused

237   by different oceans' SST anomalies; next, we eliminate the anomalies of SST forcing from a single

238   basin (Atlantic, Indian, Mediterranean, or Pacific, respectively) in the global 1950 SST/1980 SST

239   anomalies and perform simulations with the remaining SST anomalies. To obtain the effect of,

240   for instance, the 1980s Atlantic SST anomaly, we calculate the difference between Case 80SST

241   and the case, which SST anomalies is based on the global 1980s SST anomaly but without Atlantic

242   Ocean's 1980s SST anomaly. This results in consideration of both direct and indirect effects of

243   SST anomalies in the Atlantic, because when the forcing of a particular ocean SST is removed,

244   both direct and indirect effects from that ocean's anomaly are eliminated. How large the difference

245   might be or whether there is substantial difference between this and other traditional approach (i.e.,

246   adding each ocean's SST anomaly one by one) needs to be further investigated.

247   The WAMME II also includes an experiment to evaluate the sensitivity of the West African

248   climate to LULCC and to compare the effect of LULCC on the Sahel rainfall reduction with that

249   of SST anomalies. A similar strategy as in the SST experimental design, i.e., "idealized but

250   realistic" anomalies, is applied to the LULCC experiment, in which a recently available land use

251   map is employed (Hurtt et al., 2006). This map, which combines crop and pasture area change in

252   past centuries over West Africa, was derived from global land-use history products (Goldewijk,

253   2001; Ramankutty and Foley, 1999) and employed for Phase 6 of the Coupled Model

254   Intercomparison Project (CMIP6) LULCC experiment (Hurtt et al., 2011). The land map shows a

255   clear pattern of substantial land use change over the Sahel in the past century but LULCC largely

256   levels off after the 1980s (Song, 2013), which is generally consistent with the significant

257   population increase, climate effect, and conservation measures in the late last century there. This

258   part of the work is comprehensively analyzed in Boone et al. (2016, in this special issue). The

259   initial atmospheric and boundary conditions, including SST, in the LULCC experiment are the

260   same as in Case CTL in order to isolate the LULCC effect. A brief introduction of the LULCC

261   experimental design and a comparison between the LULCC experiment runs (referred to as Case

262   LULCC) and the SST runs will be discussed in Section 3.3.

263   **3). Results**

264   The impact of SST on the Sahel decadal variability and drought and its comparison with

265   the effects of LULCC are analyzed in this section. Drought has a number of generally accepted

266   definitions, such as meteorological, hydrological, agricultural, etc. The Sahel drought has already

267   been studied extensively and there is no debate concerning whether or not this was a severe drought

268   regardless of the chosen definitions. In this paper we are primarily interested in the meteorological

269 aspects of the Sahel drought, and use the precipitation reduction from the 1950s to the 1980s to

270 characterize the drought in the paper.

271 **3.1) SST Impact on the WAM Spatial Distribution and Temporal Evolution**

272 **(A). Spatial Anomaly Patterns**

273   The observed June-September (JJAS) precipitation, which is based on the CPC GTS, has

274 a clear zonal pattern with three areas associated with high precipitation: one in the West African

275 coastal area, one in the Ethiopian highlands, and another in Cameroon and Nigerian coastal areas

276 (Figure 2a and contour lines in Figure 2b). The 3-mm day^{-1} isohyet crosses the Sahel around 13ºN,

277 where Lake Chad is located. The WAMME II models (Figures 2d-2j, Figure ES1 in the Electrical

278 Supplement) produce the precipitation highs over the West African coastal area and the Ethiopian

279 highlands, as well as, except the UCONN CAM5, the high amount of precipitation near the

280 Nigerian and Cameroon coastal area but with some differences in their geographical locations. In

281 most models, the 3-mm day^{-1} zonal isohyets accurately cross Lake Chad. The UCONN CAM5's

282 3-mm day^{-1} isohyet, however, is about 2-3º north of 13ºN; while the GSFC GEOG-5 produces the

283 3-mm day^{-1} isohyet along 13ºN over West Africa. Over the eastern Sahel, however, this isohyet is

284 about 2-3º to the south of 13ºN. In the ensemble mean (Figure 2k), the two precipitation highs in

285 eastern and western Sahel, as well as the 3-mm day^{-1} isohyet along 13ºN, are adequately

286 reproduced. The high precipitation over the Nigerian and Cameroon coastal area, however, is

287 slightly weaker mostly because the precipitation high of each model have a slightly different

288 geographic location there (Figure 2k, Figure ES1L). The main WAM precipitation band reaching

289 sufficiently north is important in testing the models' response to SST and LULCC forcing. In

290 Figure 2, we display the 1-mm and 3-mm day^{-1} isohyet positions to examine the extent of the

291 boreal summertime northward migration of the primary rainfall.

292   The observed JJAS precipitation differences between the 1980s and the 1950s show a

293   severe deficit that represents the drought in the Sahel during the 1980s (Figure 2b).   The

294   observation clearly shows a meridional dipole pattern.   The areas with the most extensive

295   precipitation deficits are over the latitude band between about 10°N and 20°N, mostly to the north

296   of the 6-mm day^{-1} isohyet in the climatology. To the south of this region, i.e., along the coastal

297   area of the Bay of Guinea, there are positive anomalies (Figure 2b), which indicates that the rainfall

298   band in the 1980s was shifted to the south (Xue and Shukla, 1993); thus the northern part of the

299   monsoon precipitation band suffered the largest precipitation deficit associated with the drought.

300   According to Figure 2b, the maximum rainfall deficit was over West Africa.   The average

301   precipitation deficit between 10°N and 20°N and 10°W and 10°E, which covers most of the West

302   African severe drought area and is referred to as the Reference Area in this paper (marked by a

303   rectangle area in Fig. 2a), was 1.41 mm day^{-1}, which represents about a reduction of about 44%

304   compared with the climatology of the past 60 years (Table 2).   Meanwhile, both positive and

305   negative anomaly areas show strong spatial heterogeneity with many small peak cells.   This

306   pattern has been confirmed by the analysis based on rain gauge data and the small cells may reflect

307   the natural variability of mesoscale convective activity (Le Barbé et al., 2002) that is missed due

308   to the relatively low resolution of the GCMs.

309   Table 2 also consists of the statistics for other observational data sets, which include the

310   University of Delaware (UDel, Willmott and Matsuura, 1995) and the Climate Research Unit

311   (CRU, New et al., 1999) monthly mean precipitation data sets. These two data sets represent very

312   similar spatial precipitation differences between the 1980s and the 1950s (Appendix Figure A1)

313   but with less intensity (Table 2). Since we used the GTS data to conduct the SVD analysis, we

314   will mainly compare the simulations with the GTS data in this paper.

315   The NCEP/NCAR Reanalysis I (Figure 2c) shows a strong precipitation deficit (-1.43 mm

316   day^{-1} over the Reference Area), comparable to the observed. However, despite the generally

317   proper spatial coverage and intensity of the precipitation deficit over the Reference Area in the

318   Reanalysis climatology (except for the missing precipitation high in the Cameroon and Nigerian

319   coastal areas), the dominant drought areas are over the eastern Sahel and there is a large positive

320   anomaly in eastern Central Africa and a positive anomaly in some northern West African areas,

321   which were not found in the observation (Figure 2b, Figures A1b and c). The relative reduction

322   over the Reference Area is 51% compared with the Reanalysis climatology, higher than the

323   observed relative reduction (44%, Table 2).

324   The simulated precipitation differences between Case 80SST and Case 50SST capture

325   reasonably well the zonal rainfall deficit patterns associated with the drought with maximum

326   strength over West Africa, but with different intensities and different features of spatial distribution

327   of anomalies (Figures 2d-2j). For the WAMME II models, the precipitation reductions compared

328   to their own climatology range from 7% to 53% (Table 2). Among the models, the MRI/JMA

329   GCM, UCLA AGCM, and UCLA GFS GCM, which adequately simulate the 3 mm day^{-1} isohyet

330   (Figure 2) and intensity in model precipitation climatology (for the first two models), show the

331   larger impacts; while the NASA GEOS-5 GCM produces the least precipitation reduction over the

332   Reference Area because its main rainfall reduction area is shifted to the south of that area.

333   Nevertheless, the models show overall consistency in the positive effect of SST on rainfall

334   reduction, especially over West Africa. Due to the coarse model resolution and the lack of

335   mesoscale convective activity in GCMs, the drought patterns are much more spatially

336   homogeneous than observed. The ensemble mean (Figure 2k) indicates that with maximum SST

337   forcing, the models reproduce about 60% of the absolute amount of drought, 0.86 mm day^{-1} (Table

15

338   3), which is about a 27% reduction of the model climatology (compared with 44% reduction in

339   observation) (Table 2). It should be pointed out that the climatology of the ensemble mean's

340   precipitation is actually equal to the GTS's climatology (Table 2). In Figure 2 and the following

341   Figure 3, the absolute differences larger than 0.5 mm day^{-1} are statistically significant at $\alpha < 0.1$

342   level with a 2-tailed T-test for the SST ensemble means. When we compute the ensemble mean,

343   the GSFC GEOS-5 I and II results are averaged first to become one sample member in the

344   ensemble mean.

345   The areas with positive anomalies are much smaller in most models as well as the multi-

346   model ensemble mean than observed, mostly over the southwestern West African coast. Only the

347   ICTP-UMD model, which has the 1 mm day^{-1} isohyet reach sufficiently north and simulates three

348   precipitation highs in its climatology (Figure 2f), produces a strong dipole pattern, albeit the

349   positive anomaly is too strong in eastern Central Africa compared to the observation. However,

350   the UCLA AGCM, which also produces these features in its climatology, fails to produce the

351   dipole in West Africa at all. The SST anomaly mode imposed on the SST forcing is based on an

352   SVD analysis and the precipitation SVD1 does not show a strong positive anomaly along the

353   coastal area (Figure 1b). In addition, the SST variability associated with the interannual variability

354   was filtered as discussed in section 2. These factors may also contribute to the relatively weak

355   positive anomaly in the simulation.

356   It should be pointed out that, since we also expect other external forcings such as LULCC

357   to play a role in the decadal variability as will be discussed in Section 3.3, the rainfall reduction

358   produced by SST forcing should be weaker than observed and the simulated spatial anomaly

359   patterns may not be exactly the same as observed. However, the model results from the WAMME

16

360   II experiments seem to support a stronger SST role in the Sahel drought when compared with the

361   results from previous model inter-comparisons with SST forcing (e.g., Scaife et al., 2009).

362   The WAMME II also examines the effects of individual oceans. The relative importance

363   of SST anomalies in different basins on Sahel rainfall has still been greatly debated (Rodríguez-

364   Fonseca et al., 2015). Due to the scope of this paper, we mainly report the consensus and major

365   discrepancies of the WAMME II results on the oceans' effects. The ensemble-mean simulated

366   contributions of individual ocean basins are shown in Figures 2l-2o. The Pacific Ocean SST

367   generates the largest impact (Table 3, Figure 2o). In fact, all WAMME models produce a pattern

368   with negative anomalies (not shown) due to the Pacific SST forcing similar to their corresponding

369   ones for the global SST effects shown in Figure 2, but with less intensity. SST anomalies in the

370   Pacific alone produce about 35% of the observed precipitation reduction, with strongest effects in

371   West Africa and the western part of Central Africa. The Indian Ocean SST has the second largest

372   impact, which accounts for about 23% of the observed drought, with the main impact area over

373   the central Sahel and also the western part of Central Africa (Table 3, Figure 2m). There is an area

374   with substantial and positive precipitation anomalies over eastern Central Africa, which does not

375   have a counterpart in the observed differences between the 80s and the 50s. The WAMME models

376   show little discrepancy in the Indian Ocean SST effect. Most models produce the drought with

377   the Indian Ocean SST anomaly, with the NASA GEOS-5 being the only exception. The important

378   role of the warming trends of the Pacific and Indian SSTs in contributing to the Sahel drought

379   during the late 20th Century has been identified in a number of studies (e.g., Tippett and Giannini

380   2006; Caminade and Terray, 2010; Mohino et al., 2011; Bader and Latif, 2011), and the WAMME

381   II results are generally in line with these studies.

382   The Atlantic SST anomalies (Figure 1d), which resemble the Atlantic Niño pattern (e.g.,

383   Carton et al., 1996), result in precipitation reduction over West Africa, the central Sahel, and parts

384   of Nigeria and Cameroon and a very pronounced positive anomaly in the southwestern coastal area

385   of West Africa in the WAMME II simulation (Figure 2l).   Several papers using different

386   methodologies have shown that positive SST anomalies (Atlantic Niños) induce a dipole pattern

387   of precipitation anomalies consisting of positive values along the coast of Guinea and negative

388   ones over the Sahel (e.g., Horel et al., 1986; Wagner and Silva, 1994; Fontaine and Janicot, 1996;

389   Ward, 1998). For a warming in the Atlantic, some studies show how this dipole is the result of a

390   weakening in the sea level pressure gradient between ocean and land and, hence, in a southward

391   shift of the ITCZ from its climatological position, which translates into more rainfall over Guinea

392   and less rainfall over the Sahel. However, substantial discrepancies in simulating the Atlantic SST

393   effect among AGCM models have been reported in Losada et al. (2010). The WAMME models

394   also show quite large discrepancies in simulating Atlantic SST effects: while the GSFC GEOS-5,

395   the MRI/JMA, and the UCLA AGCM show a large impact over West Africa, the ICTP-UMD

396   GCM, the UCLA GFS, and the UCONN CAM5 show reduction in precipitation only over the

397   eastern Sahel and some positive precipitation anomalies over West Africa (Appendix Figure A2).

398   Moreover, each model shows negative anomalies but with large variability in the locations of dry

399   areas over the Reference Area, such that overall the Atlantic SST produces only a weak

400   precipitation reduction in the ensemble mean.

401   The simulated effects of Mediterranean Sea SST forcing are quite diverse among the

402   models. While the ICTP-UMD, the MRI/JMA, the UCLA AGCM, and the UCONN CAM5 show

403   negative precipitation anomalies with the Mediterranean SST, the GSFC GEOS-5 GCM and the

404   UCLA GFS show strong positive anomalies (Appendix Figure A3), which largely cancel out the

405　negative anomalies produced by the other models. Overall, the ensemble mean does not capture

406　any signal (Figure 2n). Rowell (2003) demonstrates that increased evaporation over positive SST

407　anomalies over the Mediterranean Sea leads to increased moisture content in the lower

408　troposphere, which is advected southwards into the Sahel by the low-level flow across the eastern

409　Sahara, resulting in stronger moisture convergence and precipitation over the Sahel. The negative

410　SST anomaly there should produce the opposite results. Fontaine et al (2010) also confirmed this

411　relationship. We checked each model's results and found that models that produce the dry

412　conditions with the Mediterranean SST anomaly have such a feature and models that do not show

413　the Mediterranean SST effect produced the opposite wind flow. We report the WAMME II results'

414　major discrepancies for these two ocean SST effects in this paper for a record to show the current

415　status of the state-of-the-art WAMME GCMs' performance. A comprehensive analysis of the

416　causes of these discrepancies is beyond the scope of this paper and will be the subjects of further

417　study.

418　**(B). Temporal Evolution**

419　　　SST effects are also manifested in the annual evolution of precipitation. Figures 3a and 3b

420　show the annual evolutions of the observed climatological precipitation and of the difference

421　between the 1980s and the 1950s, respectively, averaged over 10ºW and 10ºE. The annual

422　evolution of precipitation and its anomaly follows the ITCZ movement. The anomaly starts

423　developing in winter and spring. After the West African monsoon jump in late June (Figures 3a

424　and 3b), a strong dry anomaly peak appears during the summer monsoon season and the early

425　monsoon retreat; meanwhile, a positive anomaly to the south after the monsoon jump is also

426　evident. Later, in the fall, there is no substantial anomaly. The areas associated with large

427　precipitation anomalies are mostly located to the south of the 1 mm day-1 isohyet. Past studies

428   have suggested that differential heating of the northern and southern hemisphere may lead to a

429   meridional shift of the ITCZ, creating the dipole rainfall anomaly in the WAM/Sahel (Xue and

430   Shukla, 1993; Zhang and Delworth 2006; Knight et al. 2006; Ting et al. 2011). The WAMME II

431   models generally capture this anomaly evolution, albeit with significant different spatial and

432   temporal characteristics among individual models, including the Reanalysis I (Figures 3c-3j). The

433   Reanalysis I shows little latitudinal movement for both its climatology and anomalies during

434   different seasons, with negative anomalies persisting throughout the entire year over West Africa

435   and positive anomalies over southern West Africa over spring and summer (Figure 3c). The

436   evolution of the GEOS-5 II is mostly confined to the south of 10°N, while that of the UCLA

437   AGCM extends much further north of 20°N. In general, the model-simulated anomalies are

438   located to the south of the 1 mm day^{-1} isohyet. The model-produced anomalies are stronger than

439   the observed during the periods before and after the monsoon season (Figure 3d-3k), which is

440   probably due to our experimental design, i.e., imposing the same SST anomaly for every month

441   (Section 2). Another noticeable difference is that most WAMME models, except for ICTP-UMD,

442   do not show a positive precipitation anomaly in summer to the south of the Sahel. By and large,

443   the anomaly evolution process is properly produced as shown in the ensemble mean (Figure 3k),

444   but the maximum rainfall suppression during the monsoon season is weaker than observed. We

445   expect that other external forcings also contribute to the drought. Most pre-monsoon and monsoon

446   onset studies focus on May or, at the earliest, April (e.g., Sultan and Janicot, 2000). This study

447   reveals that the SST forcing produces an anomalous displacement of the ITCZ before the WAM

448   onset; the precipitation anomaly starts to develop much earlier when the ITCZ is still near the

449   equator under the SST effect. Since the WAMME II simulated annual evolution processes, the

450   results suggest a potential predictability for WAM precipitation linked to SST.

451   The effects of SST anomalies in different oceans on the anomaly evolution show different

452   characteristics. The Pacific Ocean's effect is strong mainly during the monsoon season and after

453   the retreat (Figure 3o). The average precipitation reduction over West Africa (8ºN to 20ºN and

454   10ºW to 10ºE) during June to October is 0.54 mm day^{-1}. In particular, during September and

455   October, it is 0.72 mm day^{-1}. During other seasons, the reduction over West Africa varies from

456   0.01 to 0.13 mm day^{-1}. The effects are small during the ITCZ northward movement from January

457   to May. The precipitation reduction averaged over 5ºS to 8ºN and -10ºW to 10ºE is only 0.16 mm

458   day^{-1}. The Atlantic Ocean's effect (Figure 3l) acts throughout the entire year with distinct dipole

459   patterns and intermittent pulses but is relatively weak. The role of Atlantic SST in producing this

460   dipole has been discussed in several studies (e.g., Knight et al., 2006; Mohino et al., 2011; Dieppois

461   et al., 2013). The Indian Ocean SST (Figure 3m) has the largest impact in the winter and early

462   spring during the period when the ITCZ moves northward. During January-May, the mean

463   precipitation reduction is -0.97 mm day^{-1} over 5ºS to 8ºN and 10ºW to 10ºE, then reduces to only

464   0.15 mm day^{-1} during JJAS. It has substantial impact during the WAM season; the average

465   reduction over West Africa is 0.30 mm day^{-1}. The results here suggest that variability in the Indian

466   and probably the Atlantic Ocean plays an important role in triggering the West African monsoon

467   anomaly by contributing to the ITCZ anomalous displacement and modulating atmospheric

468   circulation well before the monsoon onset, while the Pacific Ocean SST anomaly greatly

469   contributes to the summer drought. We will discuss this issue further in the mechanisms section.

470   The Pacific and the Indian Oceans' contributions over the Reference Area, on which the WAMME

471   II models have consensus, are summarized in Table 3.

472   **(C) Taylor Analyses**

473   To further quantitatively evaluate the WAMME models' performance in simulating the

474   difference between the 1980s and the 1950s precipitation, we use a Taylor diagram (Taylor 2001)

475   that encapsulates statistical comparisons of the WAMME model runs' spatial anomaly pattern as

476   well as temporal variability with the observed anomalies (Figure 4). For comparison, UDel and

477   CRU are also shown in this figure. The results in the figure are based on the June-through-

478   September monthly mean differences over the 5 years at every grid cell over the land points within

479   20°W - 30°E and 8°N - 25°N. The JJAS mean difference between Case 80SST and Case 50SST

480   for each model is removed when calculating root-mean-square-error (RMSE). Therefore, this

481   diagram does not directly show the model bias from the observed difference between the 1980s

482   and the 1950s as listed in Table 2. The position of each symbol appearing on the plot quantifies

483   how closely model's simulated and observed precipitation differences and their variability match

484   CPC GTS observations (Figure 4). The standard deviation, correlation coefficient, and RMSE are

485   used to evaluate the model's performance (See Xue et al., (2010a) for more detailed explanations

486   for the Taylor diagram analysis). The closer the model's symbol to the observation point, the

487   better the simulation is. The point representing GTS is located at the unit distance of the horizontal

488   radius (red dot in Figure 4),

489   The figure shows that models standard deviations and RMSE are close to observation. The

490   models with the best standard deviation results include the UCLA AGCM, UCONN CAM5, and

491   MRI/JMA. The GSFC GEOS-5 models exhibit the lowest standard deviations and low correlation

492   coefficients among the models because their simulated droughts areas shift to the south compared

493   with observed. The correlation coefficients for most models are in the range 0.4-0.6, which is less

494   than the correlations between GTS and other observational data sets, ~0.8. The best correlated

495   results are those generated by the ICTP-UMB and the UCONN CAM5 models, with coefficients

496 equal to 0.52 and 0.58, respectively. However, the ensemble mean shows superior performance

497 and its difference from GTS is consistent with other observational data sets. The ensemble mean's

498 RMSE, standard deviation, and correlation coefficients are 0.67, 0.9, and 0.75, respectively, which

499 is comparable to UDel's 0.62, 0.92, 0.79 and CRU's 0.62, 0.80, and 0.92, respectively. Meanwhile,

500 the Reanalysis I shows large discrepancy with the observations. Although its correlation

501 coefficient, 0.48, is similar to other models, the Reanalysis I exhibits much larger RMSE (3.85)

502 and standard deviation (4.23), as it overestimates the precipitation difference and places maximum

503 rainfall deficit to the east of the observed location. By and large, the Taylor diagram suggests that

504 the WAMME II models' results are generally quite consistent and the impacts produced by the

505 ensemble mean probably properly represent the best approximation to observations.

506

507 **3.2). Impact of SST on circulation and surface energy balance**

508   SST anomalies remotely affect WAM precipitation by modulating the regional circulation.

509 This section focuses on this modulation and changes in associated processes. As discussed in the

510 previous section, the ensemble mean represents the WAMME models' consensus on the SST effect

511 and shows its difference from the CPC GTS (after removing the bias in simulating the difference

512 between the 80s and the 50s) is comparable to other observational data sets (Figure 4); hence we

513 mainly discuss the results from the ensemble mean. In fact, WAMME I also shows that WAMME

514 multi-model ensembles have produced good WAM seasonal mean precipitation and surface

515 temperature spatial distribution, intensity, and variability, better than reanalyses in many respects

516 when compared with observations (Xue et al., 2010). Therefore, the impact characteristics shown

517 in the ensemble mean probably are more suitable to apply for interpretation of the simulated impact

518 in this study. Different characteristics of different models will be discussed only when the

519   model(s) exhibit abnormal features compared with the ensemble mean. The discussions in this

520   section emphasize the global SST results and identify the oceans that the WAMME models have

521   consensus and contribute to the major characteristics of the global SST effects. The mechanisms

522   discussed in this section will be compared with those from the LULCC effect, which will be

523   presented in the following section.

524   Low-level moisture transfer is an important feature in WAM development. The JJAS low-

525   level wind vectors and sea level pressure from the ensemble mean in Case CTL are shown in

526   Figure 5a. The relatively low sea level pressure over ~0°W to 5°E and ~20°N to 30°N is well

527   simulated. Westerly and southwesterly flow from the Atlantic brings moisture into West Africa,

528   which merges with northeasterly Harmattan winds, generating convergence in the Sahel during the

529   monsoon season. Figure 5a accurately produces the major features as shown in the NCEP

530   Reanalysis I climatology (Figure 5b). The difference between Case 80SST and Case 50SST due

531   to global SST effect shows that southwesterly flow in the West African coastal area becomes

532   weaker, northeasterly flow becomes stronger, and sea level pressure over the Sahara becomes

533   higher (Figure 5c). The NCEP Reanalysis I also shows similar features (Figure 5d), but with a

534   much larger wind and sea level pressure difference over the African continent, which may be due

535   to NCEP Reanalysis I data issue associated with sea level pressure data in 1950's and early 1960's

536   (Yang et al., 2002). To more clearly delineate the circulation change, Figure 6 shows the latitude-

537   height JJAS mean streamlines and their differences between the Case 80SST and Case 50SST

538   ensemble means. The average of zonal wind or zonal wind difference are shown in shading in

539   Figure 6 to help comprehend the following discussions.

540   Due to higher temperature over the land surfaces in the warm season, the monsoon inflow

541   is seen near the surface between 5°N and 20°N, with ascending motion across these latitudes

542   (Figure 6a), contributing to the major WAM precipitation. Meanwhile, the northerly flows that

543   occur in the middle troposphere between ~15°N and 22°N around 600 hPa as well as over the

544   region of deep convection (~5°N-10°N) at ~200-250 hPa correspond to the African easterly jet

545   (AEJ) and to the tropical easterly jet (TEJ) (Figure 6a), respectively. Those simulated features are

546   quite consistent with the Reanalysis I (Figure 6c). Compared to Case 50SST, Case 80SST has a

547   shallow layer with relatively stronger rising air between ~13°N to 20°N (Figure 6b), which is

548   associated with high surface temperature there as will be discussed later. This rising motion

549   converges with the widely spread relative sinking motion above 800 hPa, which is associated with

550   the relative divergence over most parts of the Sahel and the reduction in precipitation, enhancing

551   the northerly flow around 700 hPa. The southern flank of AEJ is enhanced and the northern flank

552   of AEJ weakens. Near the equator, the relative sinking motion induces a relative southerly flow

553   near ~200 to 300 hPa, weakening the TEJ, which is consistent with climate features in the Sahel

554   dry years: a stronger AEJ or a southward shift of its location as well as a weaker TEJ favoring

555   more precipitation over the Guinea coastal region and less precipitation over the Sahel (Xue and

556   Shukla, 1993; Cook 1999). The WAMME II ensemble mean of Case 80SST minus Case 50SST

557   correctly reproduces these climate features associated with the Sahel drought. The Reanalysis I,

558   on other hand, does not capture these features and, instead, exhibits widely spread and very strong

559   zonal wind changes (Figure 6d) that have not been reported in any analyses on WAM variability.

560   Among the WAMME II models, most produce a circulation change similar to the ensemble mean,

561   while the ICTP-UMD GCM has a distinct response with a homogeneous sinking to the north of

562   12°N and uniform rising motion to the south; no horizontal wind change appears. Among the four

563   oceans examined, the circulation changes due to the Pacific SST and Indian Ocean SST seem to

564   be more similar to the aforementioned climate features (Figures 6b, 6e, and 6f).

25

565   Moisture flux convergence and surface evapotranspiration (ET) are the main moisture

566   sources for precipitation. Reanalysis I shows the largest change in vertically integrated moisture

567   flux convergence (VIMFC), which amounts to about 80% of the simulated changes in precipitation

568   between the 80s and the 50s, and relatively low ET change amounting to about 20% (Table 2).

569   Both VIMFC and ET are model products in the Reanalysis and depend on its land model. Our

570   previous WAMME I study shows that the surface heat fluxes, including the latent heat flux, in the

571   Reanalysis products have large discrepancies with the products of the AMMA land-surface model

572   intercomparison project (ALMIP) based on the AMMA observation over West Africa (Boone et

573   al., 2010). The low ET to precipitation ratio here may result from the simple land model in

574   Reanalysis I. Our earlier studies suggest that the GCM coupled with this simple land scheme has

575   difficulties with land/atmosphere interactions (Xue et al., 2004b, 2010b). In addition, Figure 6d

576   shows that the southerly wind at ~600 hPa is enhanced in Reanalysis I in the 1980s, which is at

577   odds with the climate features during the dry years (Figure 6b). Discrepancies in producing the

578   shallow meridional circulations in the Reanalyses data in the West African region have been

579   reported (Zhang et al., 2008).

580   The reductions between Case 80SST and Case 50SST of the VIMFC and ET under global

581   SST forcing range from about 50%-80% and 50%-20%, respectively, of each WAMME II model's

582   precipitation difference (Table 2). For the model ensemble mean, VIMFC accounts for 65% of its

583   precipitation difference and ET for 35% (Table 2). Among the models, the GSFC GEOS-5 GCM

584   and UCLA AGCM show high ET/precipitation ratio, about 50%, and the UConn CAM5 shows

585   the lowest ET/precipitation ratio, (~22%). The SST anomalies affect Sahel precipitation through

586   modulating the large-scale circulation. The change in moisture transport is apparently the

587   dominant factor contributing to the precipitation difference in the WAMME models' simulations

26

588   and in the ensemble mean. Figures 7a and 7b show the JJAS VIMFC and ET differences,

589   respectively, between Case 80SST and Case 50SST for the ensemble mean. The VIMFC changes

590   between Case 80SST and Case 50SST are consistent with the circulation changes (Figures 5 and

591   6). The wide spread sinking motion between the equator and 15°N (Figure 6b) are consistent with

592   the negative VIMFC over these areas (Figure 7a); within ~12°N and 16°N and 10°W and 10E°,

593   the relative shallow rising motion (Figure 6b) compensates for this change. The spatial

594   distributions of the VIMFC difference of the ensemble mean for the global SST effect (Figure 7a)

595   and each ocean SST effect (not shown) are generally consistent with the regions of large

596   precipitation differences as shown in Figure 2 but with lower magnitude. These regions include

597   the Sahel, West African coastal area, and central Africa; while the ET changes are mostly confined

598   within the semi-arid Sahelian zone (Figure 7b). The averaged ET changes due to each ocean's

599   SST effect are around 0.1 mm day^{-1} (Table 3) and are not shown here. The annual temporal

600   evolutions of VIMFC (Figures 8a, b, c) for the global and Pacific and Indian ocean's SST effect

601   are also very much consistent with the precipitation evolution, which moves from 5°S to 20°N

602   then retreats in the annual evolution. For instance, the Indian SST effect shows large impact before

603   the monsoon season while the Pacific SST effect shows large impact during the monsoon season

604   and after the monsoon retreat. The changes of ET rates show less latitudinal movement, limited

605   to within the semi-arid area between 5°N to 20°N (Figure 8d), and large reduction occurs after the

606   monsoon season. This confirms that the change in moisture flux convergence, which is closely

607   related to the circulation change, is probably the main mechanism causing the rainfall change in

608   these experiments.

609   The SST influences the large scale circulation and MFC, which interact with cloud then

610   affecting the surface energy balances. About 90% of Sahel rainfall comes from intense, organized

611   convective activity (Mathon et al., 2002). In addition, low-level continental stratus clouds

612   frequently occur over large regions of southern West Africa during the WAM wet season (Stein et

613   al., 2011; Schrage and Fink, 2012).   Associated with the widespread relative sinking motion

614   (Figure 6b), the cloud cover in the ensemble mean is reduced in Case 80SST, especially during the

615   early spring and during the monsoon season (Figure 9a), in association with enhanced downward

616   shortwave radiation (Figure 9b). Corresponding to this enhancement, the upward shortwave

617   radiation is increased by a fraction depending on the surface albedo over the land area (north of

618   5°N) (Figure 9c). Over the ocean (south of 5°N in the figure), the change in upward shortwave

619   radiation is very small because of the low albedo. The reduction of downward longwave radiation

620   in the area to the north (~10°N to 15°N, Figure 9d) is primarily due to a decrease in cloudiness.

621   To the south of this area, there is not much change in downward longwave radiation as enhanced

622   humidity due to the rising motion near the surface layer may compensate for the effect of reduced

623   cloud cover. The upward longwave radiation changes (Figure 9e) are consistent with the surface

624   temperature changes and will be discussed next. The overall net radiation changes (Figure 9f)

625   exhibit a dipole pattern: to the south of ~10°N, the increased downward short wave radiation is

626   dominant, while to the north of this latitude, the reduced downward long wave radiation and

627   enhanced upward long wave radiation are dominant. Over the Reference Area in JJAS, the net

628   radiation reduction is 2.6 W m^{-2} for the ensemble mean, which is very different from Reanalysis

629   I, which has an increase of 8.65 W m^{-2}. Table 4 summarizes these changes in the JJAS radiation

630   component averaged over the Reference Area. The changes in annual radiation are similar to those

631   in JJAS.

632   The temporal evolution of surface temperature changes shows a dipole pattern (Figures

633   10a, b). To the north of 15°N, the reduction in net radiation is dominant such that the surface

634 temperature becomes cooler, mainly in fall, winter, and early spring. To the south, the changes in

635 surface energy balance are dominant (Table 4); the increase in surface temperature is consistent

636 with the temporal evolution of increased downward shortwave radiation (Figure 9b) and reduced

637 latent heat flux (Figure 9h). This feature appears to be quite robust as every WAMME II model

638 produces a warming over this area (Table 2), consistent with the observed warming that is based

639 on the CPC GTS data in the Sahel during the 1980s (Table 4). Based on the analyses of surface

640 temperature modes and their relationship with precipitation evolution in the WAMME I

641 experiment, we identify two summer temperature modes (Xue et al., 2010a): the Sahara mode

642 (mostly covering the Sahara area between 20°N and 30°N) and the Sahel Mode (mostly covering

643 the Sahel area between 10°N and 20°N). The crucial role of the Sahara Heat Low in WAM

644 development is well known (Lavaysse et al., 2009: Biasutti et al., 2009; Evan et al., 2015) and

645 corresponds to the Sahara mode. Meanwhile, the WAMME I results also reveal the important role

646 of another mode, the Sahel mode, and show that the summer WAM precipitation northward

647 movement/retreat is closely associated with an enhanced/weakened Sahara mode and a

648 weakened/enhanced Sahel mode. In this study, the simulated rainfall reduction due to SST effects

649 in the 1980s is also associated with the enhanced Sahel mode and weakened Sahara mode (Figures

650 10a and 10b), in agreement with the WAMME I discoveries. The observed surface temperature

651 in Sahara did not show substantial warming before the 1980s. The effects of the SST and the

652 greenhouse gases on the surface temperature over Sahara seem to have opposite sign before the

653 1980s. These two modes' changes are the results of the surface energy balance, which are closely

654 related to the circulation/cloud cover change, and also provide a feedback to the changes in WAM

655 precipitation evolution. The present study shows that such dipole changes occur not only during

656 summer (Figures 10a and 10b), but also during pre-monsoon development and monsoon retreat.

657 It is a further task to explore how changes in the pre-monsoon season contribute to changes in the

658 circulation and then the summer drought. None of the individual ocean basins seem to contribute

659 dominantly to the surface temperature anomaly patterns (not shown).

660 **3.3). Characteristics of LULCC effect**

661 In the LULCC experiment, we impose a simple LULCC scheme, which represents a

662 maximum feasible scenario. The LULCC data (Hurtt et al., 2006) are prescribed only over West

663 Africa in order to isolate the regional impacts. The areas having conversion from natural vegetation

664 cover are shown in Figure 11a, which defines the LULCC mask. We then impose a simple set of

665 land class change rules within this area, which is applied to the input land cover datasets for several

666 GCMs. After imposing the LULCC experimental scenario, broadleaf trees decrease by upwards

667 of 30%, and grasses decrease by approximately half that value; shrublands decrease in the northern

668 Sahel but increase to the south (mostly in place of decreased forest). The bare soil fraction

669 increases upwards of 30%. Consequently, these land cover changes result in corresponding

670 changes in land surface variables. For instance, the increase of local albedo reaches as high as

671 0.10 over some areas, but the average increase over the LULCC zone is approximately half of that

672 value (Figure 11b); the leaf area index (LAI) is also changed accordingly as shown in Figure 11c.

673 More comprehensive and detailed discussions on the LULCC experiment and its results are

674 presented in Boone et al., (2015, this special issue). In this paper, we show the difference between

675 Case LULCC and Case CTL, which uses a normal or climatology vegetation map, to highlight the

676 LULCC effect.

677 The JJAS precipitation differences between Case LULCC and Case CTL in Figure 12a

678 show the land forcing effect. The maximum impact is generally in the land degradation area as

679 shown in Figure 11a with West Africa having the strongest anomaly. South of this region there

680 are some positive anomalies. Since the LULCC and SST forcings produce very similar spatial

681 patterns, it is sometimes hard to distinguish the contribution of each one to the anomaly patterns

682 shown in Figure 2b. While the SST effects in most individual models and in the multi-model

683 ensemble mean feature the strongest rainfall deficit signal in the western part of Central Africa,

684 the LULCC effects feature a wet signal there. This wet signal is a feature in the observed

685 precipitation anomalies accompanying the 1980s Sahel drought that cannot result from SST effects

686 in most models. Moreover, the SST impact is apparently larger than that of the LULCC. When

687 we impose the maximum feasible forcing for each case, the SST could produce up to 60% of the

688 observed precipitation difference between the 1980s and the 1950s and LULCC produces less but

689 still a substantial amount of observed precipitation difference for the same time period, 43% (Table

690 3). In this study we use precipitation anomalies between the 1980s and the 1950s to characterize

691 the Sahel 1980s drought. In the simulations, the SST and LULCC forcings both are prescribed all

692 year long. However, in the SST experiment the precipitation anomaly starts developing from

693 winter near the equator and follows the ITCZ movement afterward (Figure 3k). In contrast, the

694 precipitation anomaly associated with the LULCC starts developing only when the precipitation

695 band moves to the region where the forcing is applied (Figure 12b), with the maximum response

696 in the summer monsoon months. These features highlight the role of SST in triggering the Sahel

697 drought and the role of land surface processes in responding to and amplifying the drought.

698   In contrast with the SST effect, the sea level pressure in Case LULCC shows no noticeable

699 changes over the Sahara but weakens over West Africa (Figure 13a). The wind from the Bay of

700 Guinea becomes weaker (Figure 13a). The circulation change due to LULCC is mainly within the

701 5°N-20°N latitude band with a very similar pattern to what the SST forcing does. A strong sinking

702 or weakened rising motion between 15°N and 20°N is presented (Figure 13b). The SST effect on

31

703 precipitation is mostly through change in VIMFC with the ratio of VIMFC and precipitation

704 change being at about 65% during the monsoon season, while in Case LULCC this ratio is about

705 54%, suggesting that local ET plays a more important role in the LULCC case (Table 3, Figure

706 14). The change in ET in Case LULCC is obviously larger than the one with SST effect (Figures

707 7b and 14b) but with no latitudinal temporal movement (Figure 14d). The LULCC affects the

708 surface energy and water balances, which then modify the large-scale circulation. Compared with

709 the SST effect, the upward short wave radiation in Case LULCC is substantially higher due to high

710 surface albedo in the land degradation areas. Thus, the net radiation decreases over the Reference

711 Area (Table 4). The reduction in latent heat flux, however, dominates the change of surface

712 temperature resulting in high surface temperature, which is similar to the SST effect over this

713 semiarid area. In contrast with the SST effect, the changes in the Sahel mode of the surface

714 temperature are dominant (Figures 12c and 12d). There is no noticeable change in the Sahara

715 mode in the LULCC experiment.

716 **4). Discussions and Conclusions**

717   The present paper presents the major results of the WAMME II SST experiment with an

718 inclusion of the comparison between impacts of SST and LULCC effects.   This is the first multi-

719 model experiment specifically designed to simultaneously evaluate the relative contribution of

720 multiple external forcings to the Sahel drought. Furthermore, the impacts of SST anomalies in the

721 world ocean as well as in individual oceans basins are examined. To test the SST effect of each

722 ocean, we subtract its SST anomaly from the global ocean forcing experiment. There is a caveat

723 in our approach in testing SST effect due to specified SST. A full assessment of these effects will

724 require using a coupled ocean-atmosphere-land model. Moreover, the results presented in this

725 study shows that due to the GCM resolution, some intra-seasonal variability, such as WAM jump,

726 as well as the spatial pattern of WAM anomaly, including its heterogeneity, are not well simulated

727 (Figure 2 and 3). Although this paper focuses on the seasonal and decadal variations, the extent

728 to which the deficiencies in intraseasonal simulation influences understanding of WAM seasonal

729 variability and its link to the decadal variability, and whether the RCMs will help the WAM

730 simulations and understanding in these aspects need further investigation.

731   The WAMME II experimental design also addresses the aerosol effects. Aerosols have

732 been proposed as a factor contributing to late 20th century drought in the Sahel via direct and

733 indirect effects (e.g., Yoshioka et al., 2007; Kim et al., 2010; Ackerley et al., 2011; Booth et al.,

734 2012; Zhang et al. 2013). The WAMME II has applied two aerosol data for the WAMME II

735 aerosol experiment: GOCART data (Chin et al., 2014) and the data from the Model of Atmospheric

736 Transport and Chemistry (Mahowald et al., 2003; Luo et al., 2003). In view of the reduced number

737 of ensemble members in the aerosol experiment, however, we have only compared the SST and

738 LULCC effects. Aerosol effects from individual model are presented in the papers by Gu et al.

739 (2015) in this special issue. More multi-model experiments on the aerosol effects are necessary to

740 allow for understand its impact.

741   In the LULCC experiment, the extent of the perturbation in the model's boundary

742 conditions is based on historical data, but heterogeneity in land degradation (Xue et al., 2004a) is

743 ignored. Furthermore, no different degrees of land degradation are considered. This experimental

744 design, therefore, may exaggerate land effects.   However, in addition to anthropogenic land use

745 change, the natural vegetation conditions also present evidence of responding to the Sahel decadal

746 rainfall variability. For instance, it has been shown that an increase in rainfall and the satellite

747 derived Normalized Difference Vegetation Index (NDVI) over the northern edge of the WAM rain

748 belt is associated with the recovery of the Sahel drought since the 1980s, when satellite data first

749 became available (Anyamba and Tucker, 2005; Herrmanna et al., 2005; Jarlan et al., 2005;

750 Govaerts and Lattanzio, 2008; Hiernaux et al. 2009; Dardel et al., 2014). The NDVI-derived leaf

751 area index (LAI) shows similar trends (Song, 2013). Although we have no observed large-scale

752 vegetation condition data before 1980, a decreasing LAI trend from the 1950s to the 1980s has

753 been confirmed and identified by a product based on a biophysical/dynamic vegetation model

754 (Figure 11d. Cox et al., 2001; Song, 2013; Zhang et al., 2015). Consistent with the LAI changes,

755 another dynamic vegetation model produces interdecadal variability in surface albedo in the Sahel

756 (Kucharski et al., 2013). Using results from a GCM, Wang et al. (2004) demonstrated that dynamic

757 vegetation-climate interactions enhance the severity of an SST-induced drought in the 2nd half of

758 the 20th century. Therefore, despite we may overestimate the LULCC situation between the 1980s

759 and the 1950s, which nevertheless is based on the best current available knowledge on this issue,

760 the land degradation due to natural vegetation variability caused by the dry trend from the 1950s

761 to the 1980s is not included. We believe that the imposed land forcing in the WAMME II should

762 provide a reasonable assessment of land effects.

763   Moreover, land surface processes include many biogeophysical and biogeochemical

764 processes, such as radiative transfer at the canopy, soil moisture, turbulence at the surface layer,

765 photosynthesis, etc. (e.g., Zeng et al., 1999; Xue et al., 2004b, 2010b; Koster et al., 2004; Ma et

766 al., 2013). The SST effects considered in this paper include the land surface biogeophysical and

767 soil moisture effects as presented in our discussions on surface water and energy balances (Figures

768 7-10). These aspects are not comprehensively investigated in the present study. More experiments

769 tackling multiple external forcings with different experiment designs are necessary to explore these

770 issues further.

771 As presented in this and other papers (e.g., Boone et al., 2015; Wang et al., 2015, in this

772 special issue), the model results submitted to the WAMME II broadly agree on the important role

773 played by SST anomalies and LULCC in WAM. Among the different ocean basins, the results

774 suggest that the Indian Ocean SST anomalies have the largest impact during the precipitation

775 anomaly development during the winter and spring, while the Pacific Ocean SST anomalies greatly

776 contribute to the summer decadal precipitation anomalies. The consensus on the global SST effect

777 on annual evolution of precipitation anomalies over West Africa suggests a potential predictability

778 of WAM development linked to SST variability. More modeling and analyses studies are

779 necessary to explore these issues further.

780 This study confirms the conjecture that the Sahel dry period in the 1980s resulted primarily

781 from remote effects of SST anomalies amplified by local land surface/atmospheric interactions.

782 The WAMME II results indicate that land surface processes are, similarly to SST, a first order

783 contributor to the Sahel drought of the 1980s and to the West African climate system in general.

784 The results of this study suggest that when each ocean's SST and land influences combine

785 synergistically to favor drought, catastrophic consequences are likely to happen in certain regions.

786 Similar phenomena have also appeared in East Asia and in the U.S. Southern Great Plains (Xue,

787 1996; Xue et al., 2005, 2016). Since the SST and land forcing in the real world are likely smaller

788 than specified in this study, further investigations on the effects of aerosols as well as of other

789 external forcings, such as greenhouse gases, and of atmospheric internal variability, are necessary.

790 It is also shown that SST and land effects share many common characteristics in affecting

791 the simulated Sahel precipitation decadal anomalies (e.g., Figures 2k and 11a, 3k and 12b, 6b and

792 13b, 7a and 14a, and 7b and 14b). This raises the difficulty of separating these two effects locally

793 in the real world. However, the outputs of WAMME II models nevertheless reveal some different

794 characteristics of how these two forcings affect the development of precipitation anomalies and

795 affect the surface energy and water balances as well as other climate features.   More

796 comprehensive observational data and analyses with more components plus modeling study should

797 help to identify and improve understanding of the natural and anthropogenic causes and guide

798 models' development and improvement.

799   Finally, although the WAMME models are broadly consistent on the effects of the global

800 SST and Pacific and Indian SST, large discrepancies exist regarding the effects of Atlantic SST.

801 Similarly, the models are unable to reach agreement on the Mediterranean SST effect. Due to the

802 scope of this paper, we mainly report the results with consensus among the WAMME II models.

803 A large number of issues that require further studies remain open. For example, why does the

804 Indian SST greatly affect the WAM onset? Also, the WAMME II results show that the models

805 have different responses to the 1950s SST and the 1980s SST (not discussed in this paper). We

806 cannot cover all these issues within the scope of this paper. We wish this paper will serve to

807 stimulate further analysis of these simulations, as well as suggest new research on different

808 external forcing's effect and dynamic and physical mechanisms contributing to the Sahel decadal

809 variability and drought. The WAMME I (Xue et al., 2010a) and this WAMME II experiment have

810 generated large amounts of data that are available for public use. The WAMME I data are available

811 at   the   NCAR   database   (openly   available   to   the   scientific   community

812 (http://data.eol.ucar.edu/master_list/?project=WAMME), and WAMME II data are available at the

813 AMMA data base (ftp.bddamma.ipsl.polytechnique.fr). The work presented only uses a small

814 portion of these data sets. More studies utilizing these data sets are highly encouraged.

815

816 **Acknowledgement**

References

Ackerley D, Booth B, Knight SHE, Highwood EJ, Frame DJ, Allen MR, Rowell DP (2011) Sensitivity of Twentieth-Century Sahel Rainfall to Sulfate Aerosol and CO2 Forcing. J. Climate 24, 4999–5014.

Anyamb, A and Tucker CJ (2005) Analysis of Sahelian vegetation dynamics using NOAA-AVHRR NDVI data from 1981–2003. Journal of Arid Environments. 63:596–614.

Bader J and Latif M (2011) The 1983 drought in the West Sahel: a case study. Climate Dyn 36:463-472.

Barnett TP (1999) Comparison of Near-Surface Air Temperature Variability in 11 Coupled Global Climate Models. J Clim 12:511–518

Benestad RE (2001) A comparison between two empirical downscaling strategies. Int J Climatol 21:1645-1668

Biasutti M, Held IM, Sobel AH, and Giannini A (2008) SST forcings and Sahel rainfall variability in simulations of the twentieth and twenty-first centuries. J. Climate, 21: 3471–3486.

Biasutti M, Sobel AH, Camargo SJ (2009) Role of the Sahara low in summertime Sahel rainfall variability in the CMIP3 models. J Clim 22:5755–5771

Boone A, Poccard-Leclerq I, Xue Y, Feng J, De Rosnay P (2010) Evaluation of the WAMME model surface fluxes using results from the AMMA land-surface model intercomparison project. In Special Issue "West African Monsoon and its Modeling" Climate Dynamics 35, 127-142. DOI 10.1007/s00382-009-0653-1

Boone A, Xue Y, De Sales F, Comer R, Hagos SM, Mahanama S, Schiro K, Song G, Wang G, Li S, Mechoso CR (2015) The regional impact of Land-Use Land-cover Change (LULCC)

845   over West Africa from an ensemble of global climate models under the auspices of the

846   WAMME2 project. Climate Dynamics, in this Special Issue, under revision.

847   Booth BB, Dunstone NJ, Halloran PR, Andrews T, Bellouin N (2012) Aerosols implicated as a

848   prime driver of twentieth-century North Atlantic climate variability. Nature 484:228-232.

849   Boyle JS (1998) Intercomparison of Interannual Variability of the Global 200-hPa Circulation for

850   AMIP Simulations. J Clim 11:2505-2529

851   Carton JA, Cao X, GieseBS, Da Silva AM (1996) Decadal and interannual SST variability in the

852   tropical Atlantic. Ocean J Phys Oceanogr 26, 1165–1175.

853   Caminade C, Terray L (2010) Twentieth century Sahel rainfall variability as simulated by the

854   ARPEGE AGCM, and future changes. Climate Dynamics 35(1):75–94.

855   doi:10.1007/s00382-009-0545-4

856   Chen M, Xie P, Janowiak JE, Arkin PA (2002) Global Land Precipitation: A 50-yr Monthly

857   Analysis Based on Gauge Observations. J Hydrometeor 3: 249-266.

858   Chin M, Rood RB, Lin SJ, M¨uller JF, Thompson AM (2000) Atmospheric sulfur cycle simulated

859   in the global model GOCART: Model description and global properties. J Geophys Res

860   105, 24671–24687.

861   Chin M, Ginoux P, Kinne S, Torres O, Holben BN, Duncan BN, Martin RV, Logan JA, Higurashi

862   A, Nakajima T (2002) Tropospheric aerosol optical thickness from the GOCART model

863   and comparisons with satellite and sun photometer measurements. J Atmos Sci 59, 461–

864   483.

865   Chin M, Diehl T, Tan Q, Prospero JM, Kahn RA, Remer LA, Yu H, Sayer AM, Bian H,

866   Geogdzhayev IV, Holben BN, Howell SG, Huebert BJ, Hsu NC, Kim D, Kucsera TL, Levy

867   RC, Mishchenko MI, Pan X, Quinn PK, Schuster GL, Streets DG, Strode SA, Torres O,

868   Zhao XP (2014) Multi-decadal variations of atmospheric aerosols from 1980 to 2009: a

869   perspective from observations and a global model. Atmos Chem Phys 14:3657-3690

870 Cook KH (1999) Generation of the African Easterly Jet and its role in determining West African

871   Precipitation. J Clim 12:1165-1184

872 Cox PM, Betts RA, Jones CD, Spall SA, Totterdell IJ (2001) Modeling vegetation and the carbon

873   cycle as interactive elements of the climate system. Meteorology at the Millenium R.

874   Pearce (ed.)

875 Dardel C, Kergoat L, Hiernaux P, Mougin E, Grippa M, Tucker CJ (2014) Re-greening Sahel: 30

876   years of remote sensing data and field observations (Mali, Niger). Remote Sens Environ

877   140: 350–364.

878 De Sales, F. Y. Xue, G. Okin (2015) Impact of burned area on the northern African seasonal

879   climate from the perspective of regional modelling, Climate Dynamics, this special issue,

880   http://link.springer.com/article/10.1007/s00382-015-2522-4

881 Dieppois B, Diedhiou A, Durand A, Fournier M, Massei N, Sebag D, Xue Y, Fontaine B (2013)

882   Quasi-decadal signals of Sahel rainfall and West African monsoon since the mid-twentieth

883   century. J Geophys Res Atmos 118 doi:10.1002/2013JD019681

884 Druyan LM, Feng J, Cook KH, Xue Y, Fulakeza M, Hagos SM, Konare A, Moufouma-Okia W,

885   Rowell DP, Vizy EK, Ibrah SS (2010) The WAMME regional model intercomparison

886   study. In Special Issue "*West African Monsoon and its Modeling*" *Climate Dynamics* **35:**

887   175-192. DOI 10.1007/s00382-009-0676-7

888 Evan AT, Flament C, Lavaysse C, Kosha C, Saci A (2015) Water Vapor–Forced Greenhouse

889   Warming over the Sahara Desert and the Recent Recovery from the Sahelian Drought. J

890   Climate 28:108-123.

891 Folland C, Owen J, Ward MN, Colman A (1991) Prediction of seasonal rainfall in the Sahel region

892 using empirical and dynamical methods. J Forecasting 1, 21-56.

893 Fontaine B, Janicot S (1996) Sea surface temperature fields associated with West African rainfall

894 anomaly types. J Clim 9:2935–2940.

895 Fontaine B, Roucou P, Sivarajan S, Gervois S, Chauvin F, Rodriguez de Fonseca MB, Ruti P,

896 Janicot S (2010) Impacts of Warm and Cold situations in the Mediterranean Basins on the

897 West African monsoon: observed connection patterns (1979-2006) and climate

898 simulations. Climate Dynamics 35:95–114 DOI 10.1007/s00382-009-0599-3

899 Giannini A, Saravanan R, Chang P (2003) Oceanic forcing of Sahel rainfall on interannual to

900 interdecadal time scales. Science 302, 1027–1030.

901 Goldewijk KK (2001) Estimating global land use change over the past 300 years: the HYDE

902 database. Global Biogeochemical Cycles 15, 417–433.

903 Govaerts YM and Lattanzio A (2008) Estimation of surface albedo increase during the eighties

904 Sahel drought from Meteosat observations. Global and Planetary Change. 64:139-145, doi

905 10.1016/j.gloplacha.2008.04.004.

906 Gu Y, Xue Y, De Sales F, Liou KN (2015) A GCM Investigation of Dust Aerosol Impact on

907 Regional Climate of North Africa and South/East Asia. Climate Dynamics, in this Special

908 Issue, http://link.springer.com/article/10.1007/s00382-015-2706-y

909 Hagos SM, Cook KH (2008) Ocean Warming and Late-Twentieth-Century Sahel Drought and

910 Recovery. J Climate 21:3797-3814.

911 Hagos S, Leung LR, Xue Y, Boone A, De Sales F, Neupane N, Huang M, Yoon JH (2014)

912 Assessment of Uncertainties in the Response of the African Monsoon Precipitation to Land

Use Change simulated by a Regional Model. Climate Dynamics 43:2765-2775 DOI 10.1007/s00382-014-2092-x

HastenrathS, Polzin D (2010) Long-term variations of circulation in the tropical Atlantic sector and Sahel rainfall. Int J Climatology. 31(5):649-655 DOI: 10.1002/joc.2116

Herrmanna, SM, Anyambab A, Tucker CJ (2005) Recent trends in vegetation dynamics in the African Sahel and their relationship to climate. Global Environmental Change. 15:394–404.

Hiernaux P, Diarra L, Trichon V, Mougin E, Soumaguel N, Baup F (2009) Woody plant population dynamics in response to climate changes from 1984 to 2006 in Sahel (Gourma, Mali). Journal of Hydrology, 375 (1-2): 103-113.

Hoerling M, Hurrell J, Eischeid J, Phillips A (2006) Detection and attribution of twentieth-century northern and southern African rainfall change. J Clim 19: 3989-4008

Hoerling, M, Eisheid J, Perlwitz J (2010) Regional Precipitation Trends: Distinguishing Natural Variability from Anthropogenic Forcing. J Climate 23:2131-2145.

Horel JD, Kousky VE, Kagano MT (1986) Atmospheric conditions in the Atlantic sector during 1983 and 1984. Nature 322:6076, 248-251.

Hourdin F, Musat I, Grandpeix J-Y, Polcher J, Guichard F, Favot F, Marquet P, Boone A, Lafore J-P, Redelsperger J-L, Ruti PM, Dell'aquila A, Filiberti MA, Pham M, Doval TL, Traore AK, Gallée H (2010) AMMA-Model Intercomparison Project. Bull Amer Meteor Soc 91:95–104 doi: http://dx.doi.org/10.1175/2009BAMS2791.1

Hurtt GC, Frolking S, Fearon MG, Moore B, Shevliakova E, Malyshev S, Pacala SW, Houghton RA (2006) The underpinnings of land-use history: three centuries of global gridded land-

935 use transitions, wood harvest activity, and resulting secondary lands. Global Change Biol

936   12:1208–1229

937 Hurtt GC, Chini LP, Frolking S, Betts R, Feddema J, Fischer G, Fisk JP, Hibbard K, Houghton

938   RA, Janetos A, Jones C, Kindermann G, Kinoshita T, Klein Goldewijk K, Riahi K,

939   Shevliakova E, Smith S, Stehfest E, Thomson A, Thornton P, van Vuuren DP Wang Y

940   (2011) Harmonization of Land-Use Scenarios for the Period 1500-2100: 600 Years of

941   Global Gridded Annual Land-Use Transitions, Wood Harvest, and Resulting Secondary

942   Lands. Climatic Change 109:117–161. doi :10.1007/s10584-011-0153-2.

943 Janicot S, Harzallah A, Fontaine B, Moron V (1998) West African Monsoon Dynamics and

944   Eastern Equatorial Atlantic and Pacific SST Anomalies (1970–88). J Climate 11:184-1882.

945 Jarlan L, Tourre YM, Mougin E, Philippon N, and Massega P (2005) Dominant patterns of

946   AVHRR NDVI interannual variability over the Sahel and linkages with key climate signals

947   (1982–2003). Geophy. Res. Let. 32: L04701, doi:10.1029/2004GL021841

948 Joly M, Voldoire A, Douville H, Terray P, Royer JF (2007) African monsoon teleconnections with

949   tropical SSTs: validation and evolution in a set of IPCC4 simulations Clim Dyn

950   DOI:0.1007/s00382-006-0215-8.

951 Kanamitsu M, Ebisuzaki W, Woollen J, Yang SK, Hnilo JJ, Fiorino M, Potter GL (2002a) NCEP–

952   DOE AMIP-II Reanalysis (R-2). Bull Am Meteorol Soc 83:1631−1643

953 Kanamitsu M, Kumar A, Juang HMH, Wang W, Yang F, Schemm J, Hong SY, Peng P, Chen W,

954   Ji M (2002b) NCEP Dynamical Seasonal Forecast System 2000. Bull Am Meteorol Soc

955   83:1019-1037

956 Kim KM, Lai WKM, Sud YC, Walker GK (2010) Influence of aerosol-radiative forcings on the

957   diurnal and seasonal cycles of rainfall over West Africa and Eastern Atlantic Ocean using

958   GCM simulations. Clim Dyn (35), 115-126.

959 Knight JR, Folland CK, Scaife AA (2006) Climate impacts of the Atlantic Multidecadal

960   Oscillation. Geophys Res Lett 33: doi:10.1029/2006GL026242

961 Koster R, Suarez MJ, Ducharne A, Kumar P, Stieglitz M (2000) A catchment based approach to

962   modeling land surface processes in a GCM—Part 1: Model structure. J Geophys Res

963   105:809–822

964 Koster RD, Dirmeyer PA, Guo Z, Bonan G, Chan E, Cox P, Gordon CT, Kanae S, Kowalczyk E,

965   Lawrence D, Liu P, Lu CH, Malyshev S, McAvaney B, Mitchell K, Mocko D, Oki T,

966   Oleson K, Pitman A, Sud YC, Taylor CM, Verseghy D, Vasic R, Xue Y, Yamada T (2004)

967   Regions of strong coupling between soil moisture and precipitation. Science 305, 1138-

968   1140.

969 Kucharski F, Zeng N, Kalnay E (2013) A further assessment of vegetation feedback on decadal

970   Sahel rainfall variability. Climate Dyn 40:1453–1466 doi:10.1007/s00382-012-1397-x.

971 Lamb P J (1978) Large-scale tropical Atlantic surface circulation patterns associated with sub-

972   Saharan weather anomalies. Tellus 30:240-251

973 Lau K M, Shen SSP, Kim KM, Wang H (2006) A multimodel study of the twentieth-century

974   simulations of Sahel drought from the 1970s to 1990s. J Geophys Res 111: D07111

975   doi:10.1029/2005JD006281.

976 Lavaysse C, Flamant C, Janicot S, Parker DJ, Lafore JP, Sultan B, Pelon J (2009) Seasonal

977   evolution of the West African heat low: A climatological perspective. Climate Dyn **33:**

978   313–330.

979   Le Barbé L, Lebel T, Tapsoba D (2002) Rainfall variability in West Africa during the years 1950–

980   90. J Clim 15:187–202.

981   Lebel T, Ali A (2009) Recent trends in the Central and Western Sahel rainfall regime 1990–2007

982   Journal of Hydrology 375:52–64

983   Losada T., Rodríguez-Fonseca S, Janicot S, Gervois S, Chauvin F, and Ruti P (2010) A multi-

984   model approach to the Atlantic equatorial mode: Impact on the West African monsoon.

985   Climate Dyn., 35, 29–43, doi:10.1007/s00382-009-0625-5.

986   Lu, J, Delworth TL (2005) Oceanic forcing of the late 20th century Sahel drought. Geophys Res

987   Lett 32 L22706 doi:10.1029/2005GL023316.

988   Luo C, Mahowald N, Del Corral J (2003) Sensitivity study of meteorological parameters on

989   mineral aerosol mobilization, transport and distribution. J Geophys Res 108, D15, 4447,

990   10.1029/2003JD0003483.

991   Ma HY, Mechoso CR, Xue Y, Xiao H, Neelin JD, Ji X (2013) On the connection between

992   continental-scale land surface processes and the tropical climate in a coupled ocean-

993   atmosphere-land system. J Climate 26, 9006-9025

994   http://journals.ametsoc.org/doi/pdf/10.1175/JCLI-D-12-00819.1

995   Mahowald N, Luo C, Del Corral J, Zender C (2003) Interannual variability in atmospheric mineral

996   aerosols from a 22-year model simulation and observational data. JGR 108 (D12),

997   10.1029/2002JD002821.

998   Martin ER, Thorncroft C (2014), Sahel rainfall in multimodel CMIP5 decadal hindcasts. Geophys

999   Res Lett (41): 2169–2175 doi:10.1002/2014GL059338.

1000   Mathon V, Laurent H, Lebel T (2002) Mesoscale convective system rainfall in the Sahel. J Appl

1001   Meteorol 41:1081–1092.

1002   Mechoso CR, Yu JY, Arakawa A (2000) A coupled GCM pilgrimage: From climate catastrophe

1003   to ENSO simulations. General circulation model development: Past, present and future.

1004   Proceedings of a Symposium in Honor of Professor Akio Arakawa, D. A. Randall.

1005   Academic Press, USA, pp 539-575

1006   Mizuta R, Oouchi K, Yoshimura H, Noda A, Katayama K, Yukimoto S, Hosaka M, Kusunoki S,

1007   Kawai H, Nakagawa M (2006) 20-km-mech global climate simulations using JMA-GSM

1008   model, Mean Climate States. J Meteorol Soc Japan 84:165-185

1009   Mohino E, Janicot S, Bader J (2011) Sahel rainfall and decadal to multi-decadal sea surface e

1010   temperature variability. Clim Dyn 37:419-440 doi:10.1007/s00382-010-0867-2.

1011   Molod A, Takacs LL, Suarez MJ, Bacmeister JT, Song IS, Eichmann A (2012) The GEOS-5

1012   Atmospheric General Circu- lation Model: Mean Climate and Development from MERRA

1013   to Fortuna. NASA Tech. Memo. 104606, Vol. 28, Tech. Rep. Series on Global Modeling

1014   and Data Assimilation, edited by: Suarez, M. J., 117 pp.

1015   Neale RB, Chen CC, Gettelman A et al. (2012) Description of the NCAR Community Atmosphere

1016   Model (CAM 5.0), Technical Note NCAR/TN-486+STR. National Center for Atmospheric

1017   Research, Boulder, Colorado, 274pp.

1018   New, M., Hulme, M. and Jones, P.D. (1999): Representing twentieth century space-time climate

1019   variability. Part 1: development of a 1961-90 mean monthly terrestrial climatology. Journal

1020   of Climate 12:829-856.

1021   Nicholson SE, Dezfuli AK, and Klotter D (2012) A Two-Century Precipitation Dataset for the

1022   Continent   of   Africa.   Bull.   Amer.   Meteor.   Soc.,   93:1219–1231.

1023   doi:http://dx.doi.org/10.1175/BAMS-D-11-00212.1

1024   Pope VD, Gallani ML, Rowntree PR, Stratton RA (2000) The impact of new physical
1025   parametrizations in the Hadley Centre climate model: HadAM3. Clim Dyn 16:123–14

1026   Ramankutty N, Foley JA (1999) Estimating historical changes in global land cover: croplands from
1027   1700 to 1992. Global Biogeochemical Cycles, 13: 997–1027.

1028   Rayner NA, Parker DE, Horton EB, Folland CK, Alexander LV, Rowell DP, Kent EC, Kaplan A
1029   (2003) Global analyses of sea surface temperature, sea ice, and night marine air
1030   temperature since the late nineteenth century. J Geophys Res 108: D14 doi:4407
1031   10.1029/2002JD002670

1032   Redelsperger JL, Thorncroft CD, Diedhiou A, Lebel T, Parker DJ, Polcher J (2007) American
1033   monsoon multidisciplinary analysis. Bull Amer Meteor Soc 88, 1740-1746.

1034   Rodriguez-Fonseca B, Mohino E, Mechoso CR, Caminade C, Biasutti M, Gaetani M, García-
1035   Serrano J, Vizy EK, Cook K, Xue Y, Polo I, Losada T, Druyan L, Fontaine B, Bader J,
1036   Doblas-Reyes FJ, Goddard L, Janicot S, Arribas A, Lau W, Colman A, Rowell DP,
1037   Kucharski F, Voldoire A (2015) Variability and Predictability of West African Droughts.
1038   J Climate 28, 4034-4060

1039   Roehrig R, Bouniol D, Guichard F, Hourdin F, Redelsperger JL (2013) The present and future of
1040   the West African monsoon: a process-oriented assessment of CMIP5 simulations along the
1041   AMMA transect. J. Climate. 26, 6471–6505. doi: 10.1175/JCLI-D-12-00505.1

1042   Rowell DO (2001) Teleconnections between the Tropical Pacific and the Sahel. Q J R Meteorol
1043   Soc 127:1683-1706.

1044   Rowell DO (2003) The Impact of Mediterranean SSTs on the Sahelian Rainfall Season. J Climate
1045   16:849-8610.

1046   Scaife A, Kucharski F, Folland C, Kinter III J, Fereday D, Fischer A, Grainger S, Jin E, Kang I,

1047   Knight J, Kusunoki S, Lau N, Nath M, Nakaegawa T, Pegion P, Schubert S, Sporyshev P,

1048   Syktus J, Yoon J, Zeng N, Zhou T (2009): The CLIVAR C20C Project: Selected 20th

1049   century climate events. Climate Dynamics 33:603-614 doi:10.1007/s00382-008-0451-1.

1050   Schrage JM, Fink AH (2012) Nocturnal Continental Low-Level Stratus over Tropical West Africa:

1051   Observations and Possible Mechanisms Controlling Its Onset. Mon Weather Rev 140:

1052   doi:10.1175/MWR-D-11-00172.1.

1053   Sengupta S, Boyle JS (1998) Using common principal components in comparing GCM

1054   simulations. J Clim 11:816–830

1055   Song G (2013) Global and Sahel Regional Biophysical Processes, Vegetation Dynamics, and

1056   Climate Interactions. Ph.D. Dissertation. University of California, Los Angeles PP 183.

1057   Stein THM, Parker DJ, Delanoë J, Dixon NS, Hogan RJ, Knippertz P, Maidment RI, Marsham JH

1058   (2011) The vertical cloud structure of the West African monsoon: A 4 year climatology

1059   using CloudSat and CALIPSO. J Geophys Res 116: D22205 doi:10.1029/2011JD016029.

1060   Stouffer RJ, Hegerl G, Tett S (2000) A comparison of surface air temperature variability in three

1061   1000-yr coupled ocean-atmosphere model integrations. J Clim 13:513-537

1062   Sultan B, Janicot S (2000) The West African Monsoon Dynamics. Part II: The ''Preonset'' and

1063   ''Onset'' of the Summer Monsoon. J Climate 16:3407-3427.

1064   Ting M, Kushnir Y, Seager R, Cuihua L (2011) Robust features of Atlantic multi-decadal

1065   variability   and   its   climate   impacts.   Geophys   Res   Lett   38:   L17705

1066   doi:10.1029/2011GL048712

1067   Tippett MK, Giannini A (2006) Potentially predicable components of African summer rainfall in

1068   an SST-forced GCM simulation. J Climate 19:3133-3144.

1069 Wagner RG, Da Silva AM (1994) Surface conditions associated with anomalous rainfall in the
1070   Guinea coastal region. Int J Climatol 14:179–199.

1071 Wallace JM, Smith C, Bretherton CS (1992) Singular value decomposition of wintertime sea
1072   surface temperature and 500-mb height anomalies J Climate 5:561-576.

1073 Wang GL, Eltahir EAB, Foley JA, Pollard D, Levis S (2004) Decadal variability of rainfall in the
1074   Sahel: results from the coupled GENESIS-IBIS atmosphere-biosphere model. Climate
1075   Dynamics, 22(6-7):625-637, doi: 10.1007/s00382-004-0411-3

1076 Wang GL, Yu M, Xue Y (2015) Modeling the potential contribution of land use changes to the
1077   20th Century Sahel drought using a regional climate model: Impact of lateral boundary
1078   conditions. Climate Dynamics in this Special Issue, DOI 10.1007/s00382-015-2812-x.

1079 Ward M N (1998) Diagnosis and short-lead time prediction of summer rainfall in tropical North
1080   Africa at interannual and multidecadal timescales. J Climate 11:3167–3191.

1081 Weng HY, Lau KM, and Xue YK (1999) Long term variations of summer rainfall over China and
1082   its possible link to global sea-surface temperature variability. J. Meteor. Soc. Of Japan,
1083   77, 845-857.

1084 Willmott CJ, Matsuura K (1995) Smart interpolation of annually averaged air temperature in the
1085   United States. Journal of Applied Meteorology, 34, 2577-2586.

1086 Xue Y, Shukla J (1993) The influence of land surface properties on Sahel climate. **Part I:**
1087   Desertification. J Climate **6:** 2232-2245.

1088 Xue Y (1996) The Impact of desertification in the Mongolian and the Inner Mongolian grassland
1089   on the regional climate. J Climate 9: 2173-2189.

1090 Xue Y, Hutjes RWA, Harding RJ, Claussen M, Prince S, Lambin EF, Allen SJ, Dirmeyer P, Oki
1091   T (2004a) The Sahelian Climate (Chapter A5) in Vegetation, Water, Humans and the

1092   Climate, Eds, P. Kabat, M. Claussen, P. A. Dirmeyer, et al., Springer-Verlag, Berlin

1093   Heidelberg, P59-77.

1094 Xue Y, Juang HM, Li W, Prince S, DeFries R, Jiao Y, Vasic R (2004b) Role of land surface

1095   processes in monsoon development: East Asia and West Africa. J Geophys Res 109:

1096   D03105. doi:10.1029/2003JD003556

1097 Xue Y., Sun S, Lau JM, Ji J, Poccard I, Kang HS, Zhang R, Wu G, Zhang J, Schaake J, Jiao Y

1098   (2005) Multiscale variability of the river runoff system in China and its link to precipitation

1099   and sea surface temperature. J Hydrometeorology 6:550-570.

1100 Xue Y, De Sales F, Lau KMW, Boone A, Feng J, Dirmeyer P, Guo Z, Kim KM, Kitoh A, Kumar

1101   V, Poccard-Leclercq I, Mahowald N, Moufouma-Okia W, Pegion P, Rowell D, Schubert

1102   SD, Sealy A, Thiaw WM, Vintzileos A, Williams S, Wu MLC (2010a) Intercomparison

1103   and analyses of the climatology of the West African Monsoon in the West African

1104   Monsoon Modeling and Evaluation Project (WAMME) First Model Intercomparison

1105   Experiment. In Special Issue "West African Monsoon and its Modeling" Climate

1106   Dynamics 35:3- 27 DOI: 10.1007/s00382-010-0778-2.

1107 Xue Y., De Sales F, Vasic R, Mechoso CR, Prince SD, Arakawa A (2010b) Global and temporal

1108   characteristics of seasonal climate/vegetation biophysical process (VBP) interactions. J

1109   Climate 23:1411−1433.

1110 Xue Y, Boone A, Taylor CM (2012) Review of Recent Developments and the Future Prospective

1111   in West African Atmosphere/Land Interaction Studies in the Special Issue "Advances in

1112   Climate Processes, Feedbacks, Variability, and Change for the West African Climate

1113   System" International Journal of Geophysics 2012: doi:10.1155/2012/748921.

Xue Y, Oaida CM, Diallo I, Neelin JD, Li S., De Sales F., Gu Y., Robinson D., Vasic R. and Yi L. (2016) Spring land temperature anomalies in northwestern US and the summer drought over Southern Plains and adjacent areas, Environ. Res. Lett. 11, 044018, http://dx.doi.org/10.1088/1748-9326/11/4/044018

Yang S, Lau KM, Kim KM. (2002) Variations of the East Asian jet stream and Asian – Pacific – American winter climate anomalies. Journal of Climate 15: 306 – 325

Yoshioka M, Mahowald NM, Conley AJ, Collins WD, Fillmore DW, Zender CS, Coleman DB (2007) Impact of Desert Dust Radiative Forcing on Sahel Precipitation: Relative importance of dust compared to sea surface temperature variations, vegetation changes and greenhouse gas warming. J Clim 20:1445-1467

Zeng N, Neelin JD, Lau KM, Tucker CJ (1999) Enhancement of interdecadal climate variability in the Sahel by vegetation interaction. Science 286:1537-1540

Zhang C, Nolan DS, Thorncroft CD (2008) Shallow Meridional Circulations in the Tropics Represented by Global Reanalyses. J Climate 21:3453-3470.

Zhang R, Delworth TL (2006) Impact of Atlantic multidecadal oscillations on India/Sahel rainfall and Atlantic hurricanes. Geophys Res Lett 33: L17712 doi:10.1029/2006GL026267.

Zhang R, Delworth TL, Sutton R, Hodson DLR, Dixon KW, Held IM, Kushnir Y, Marshall J, Ming Y, Msadek R, Robson J, Rosati AJ, Ting M, Vecchi GA (2013) Have Aerosols Caused the Observed Atlantic Multidecadal Variability? J Atmos Sci 70:1135–1144 doi: http://dx.doi.org/10.1175/JAS-D-12-0331.

Zhang Z, Xue Y, MacDonald G, Cox PM, Collatz GJ (2015) Investigation of North American vegetation variability under recent climate – A study using the SSiB4/TRIFFID

1136   biophysical/dynamic vegetation model.   J Geophy Res. 120: 1300–1321.   DOI:

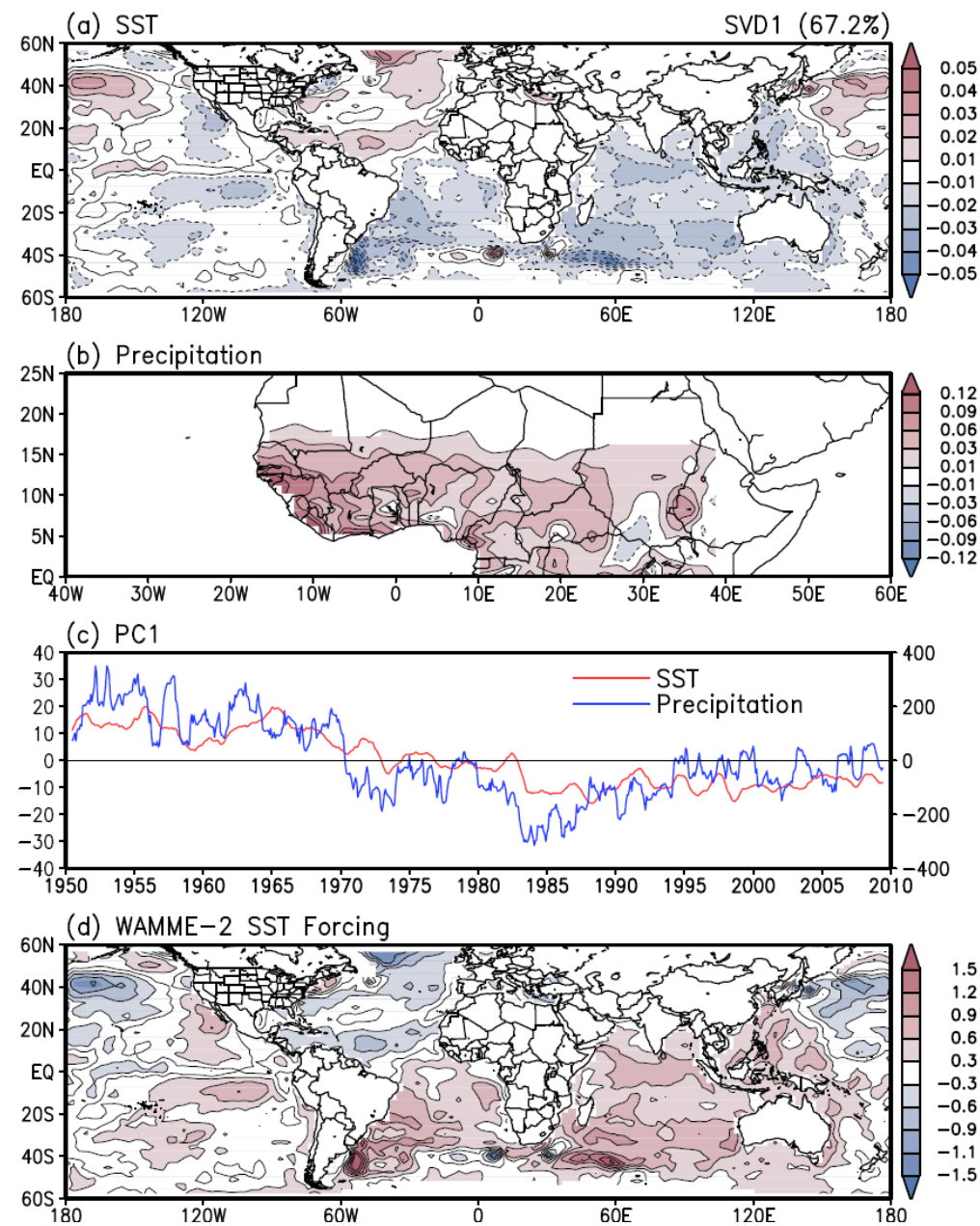1137   10.1002/2014JD021963

Figure Captions

Figure 1. (a, b) SST and precipitation SVD1 spatial patterns; (c) SVD PC1 time series during the

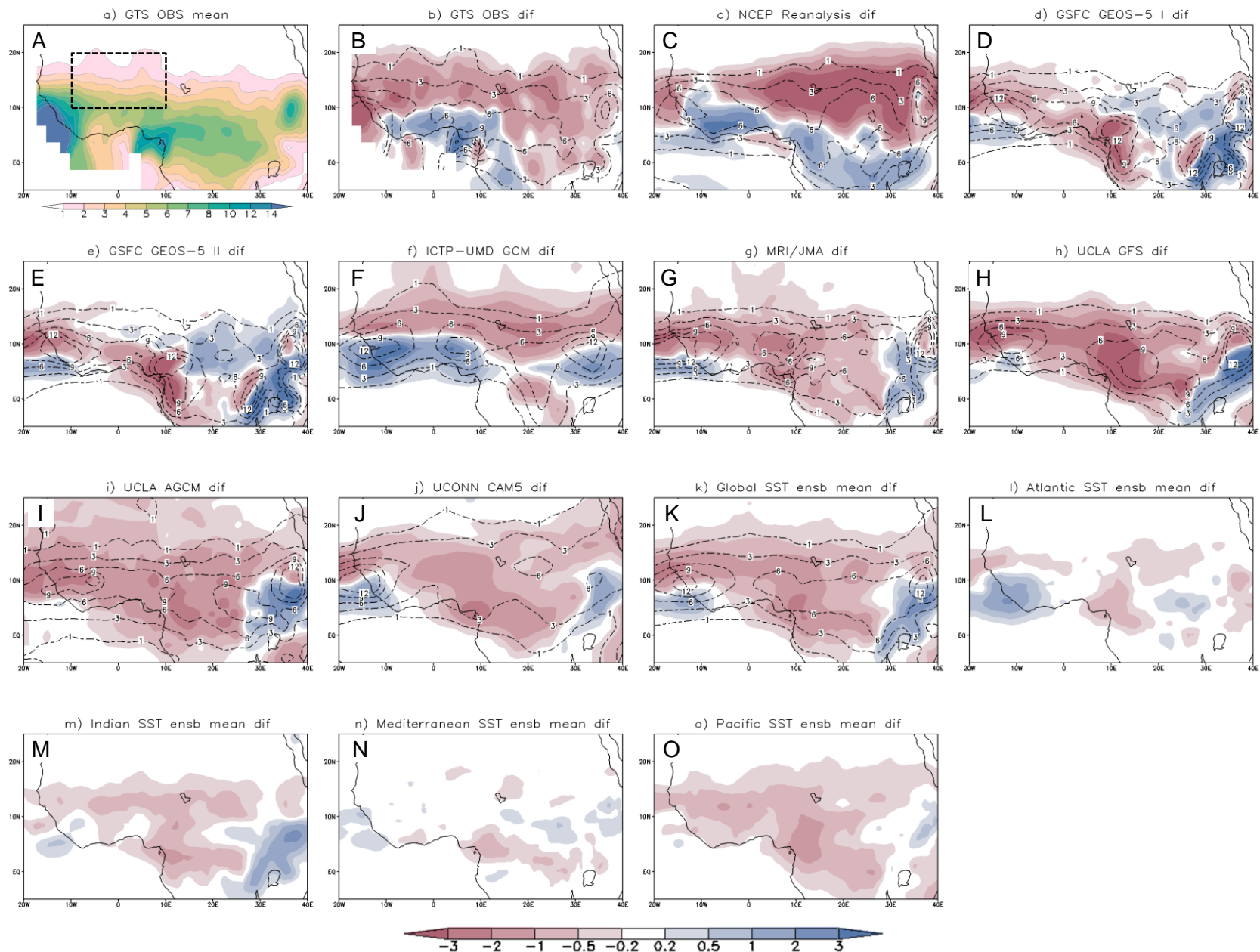1950–2010 period; (d) WAMME SST forcing difference between 1980s and 1950s (°C)

Figure 2. JJAS mean observed and simulated precipitation (mm day^{-1}): (a) GTS climatology; (b)

GTS precipitation difference between the 1980s and the 1950s; (c) Reanalysis I precipitation

difference between the 1980s and the 1950s; (d)-(j) individual model simulated difference between

Case 1980SST and Case 1950SST; (k) ensemble mean difference for global SST effect; (l)-(o)

ensemble mean for each ocean basin effect. The corresponding climatology from observation and

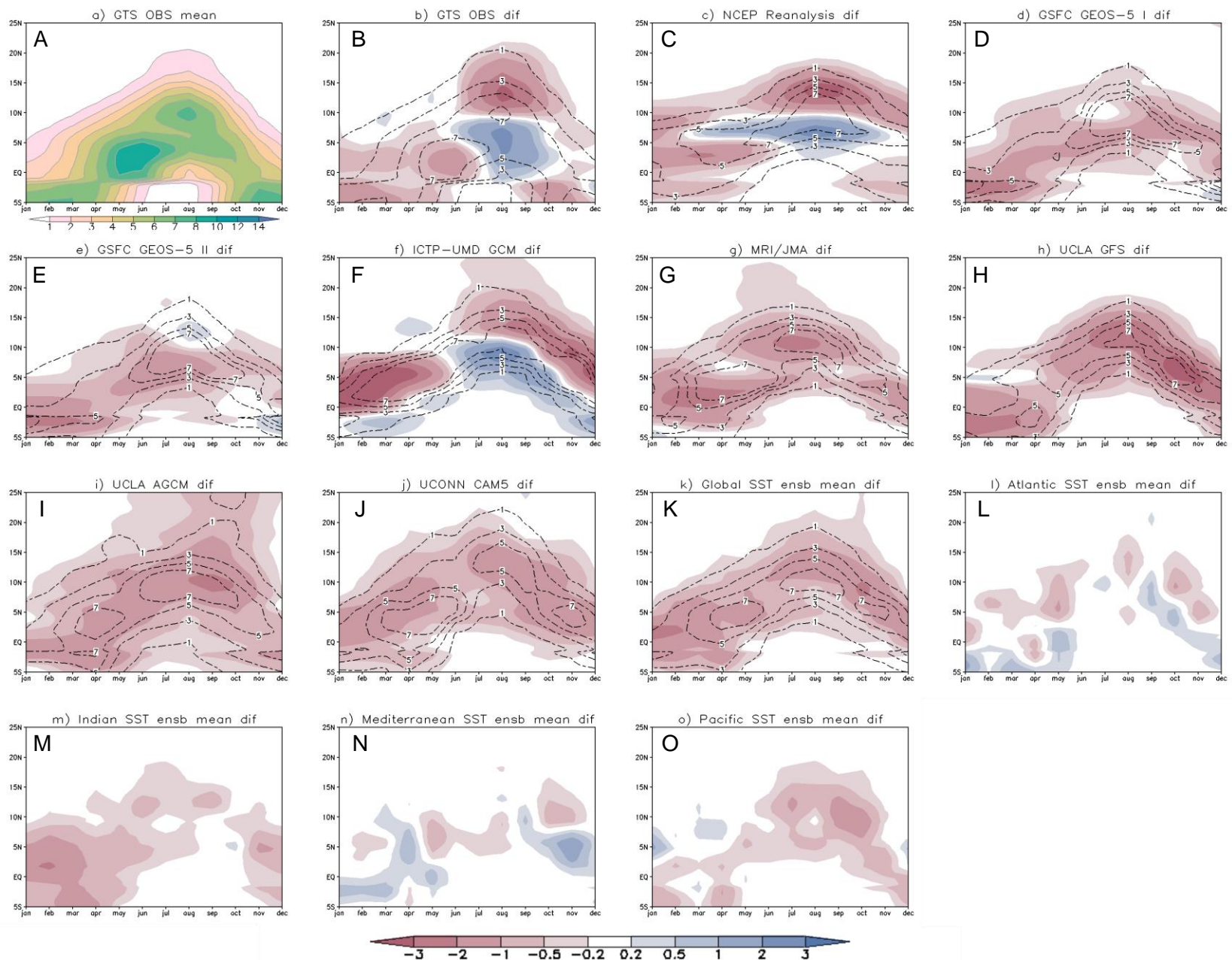simulations for each model are displayed as contour lines in (b)-(k).

Figure 3. Observed and simulated precipitation temporal evolution (mm day^{-1}): (a) GTS

climatology; (b) GTS precipitation difference between the 1980s and the 1950s; (c) Reanalysis I

precipitation difference between the 1980s and the 1950s; (d)-(j) individual model simulated

difference between Case 1980SST and Case 1950SST; (k) ensemble mean difference for global

SST effect; (l)-(o) ensemble mean difference for each ocean basin effect. The corresponding

climatology from observation and simulations for each model are displayed as contour lines in
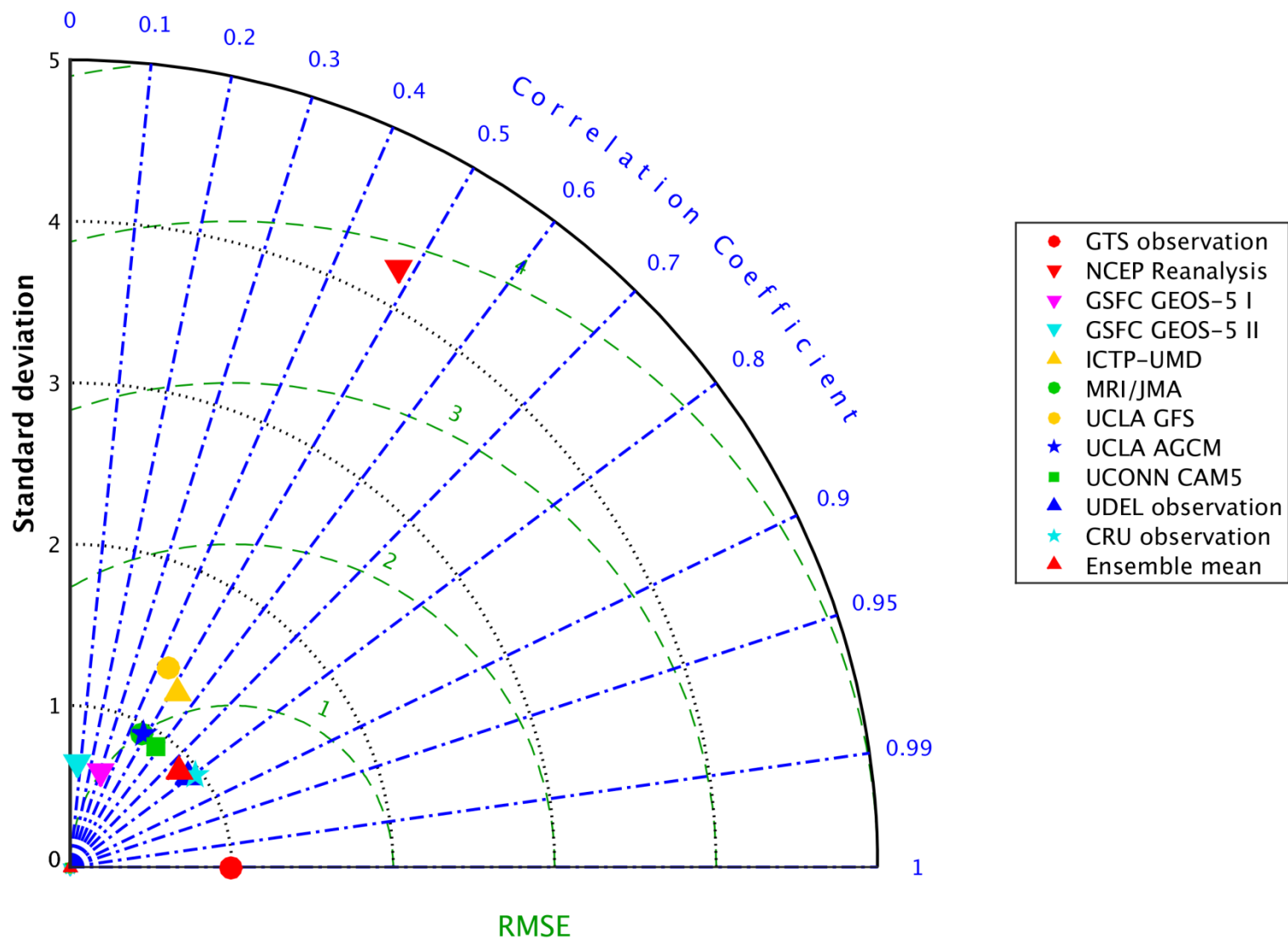
(b)–(k).

Figure 4. Taylor diagram for JJAS precipitation anomaly.

1161   Figure 5. Simulated JJAS mean and anomalies of 950 hPa wind vectors (m s^{-1}) and SLP (hPa): (a)

1162   Case CTL ensemble mean; (b) NCEP Reanalysis climatology; (c) Case 80SST – Case 50SST

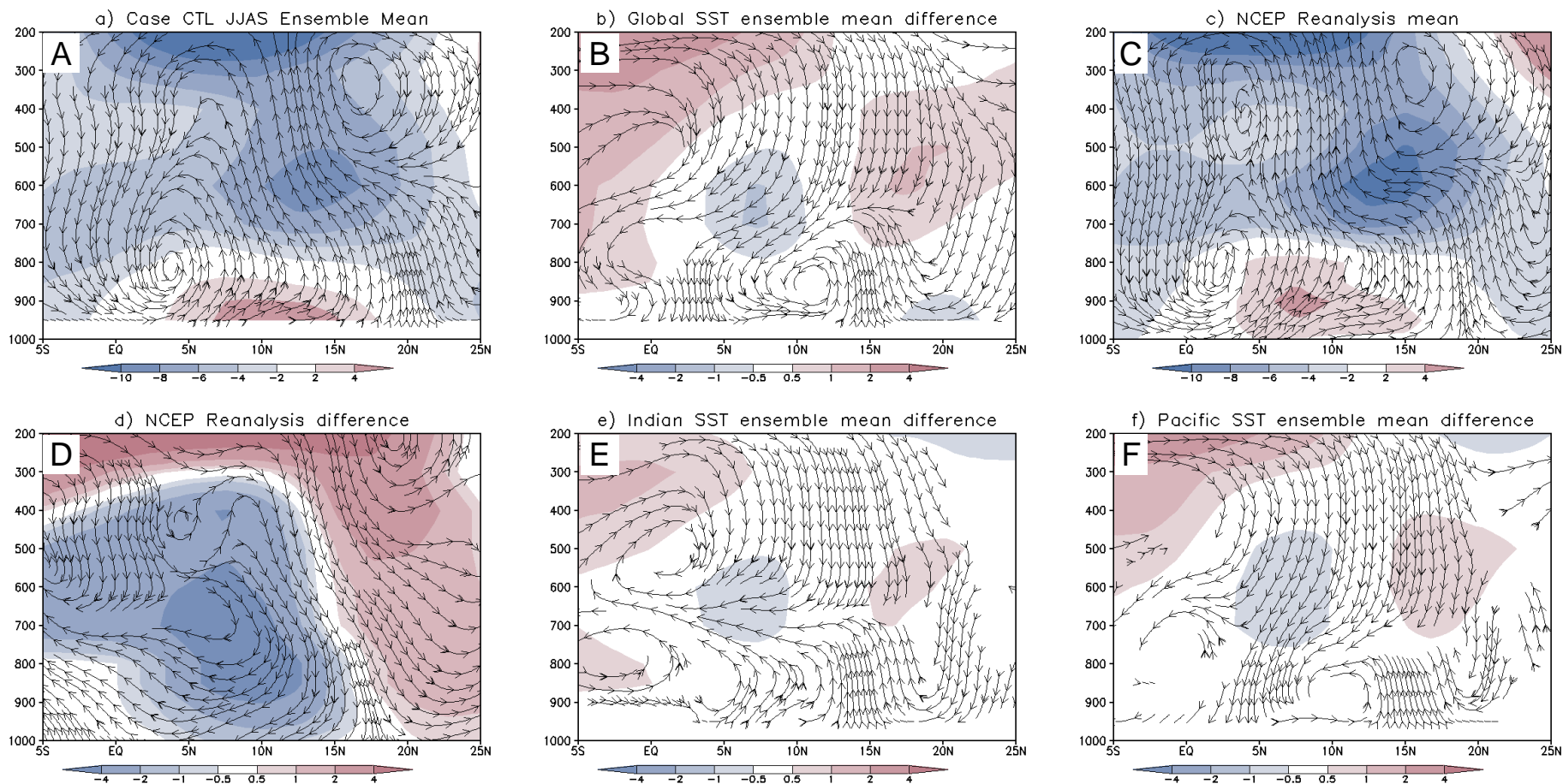1163   ensemble mean; (d) NCEP Reanalysis difference between the 1980s and the 1950s

1164

1165   Figure 6. Latitude-height cross section of JJAS mean and anomaly streamline (v, -100*w)

1166   averaged between 10°W and 10°E: (a) Case CTL ensemble; (b) Case 80SST – Case 50SST

1167   ensemble mean; (c) NCEP reanalysis climatology; (d) NCEP Reanalysis difference between the

1168   1980s and the 1950s; (e) Indian Ocean SST effect; (f) Pacific Ocean SST effect. Note: The average

1169   of zonal wind or zonal wind differences are in shade (m s^{-1})
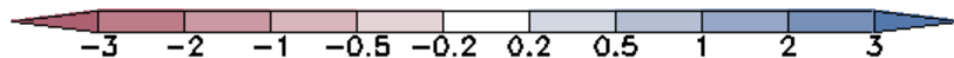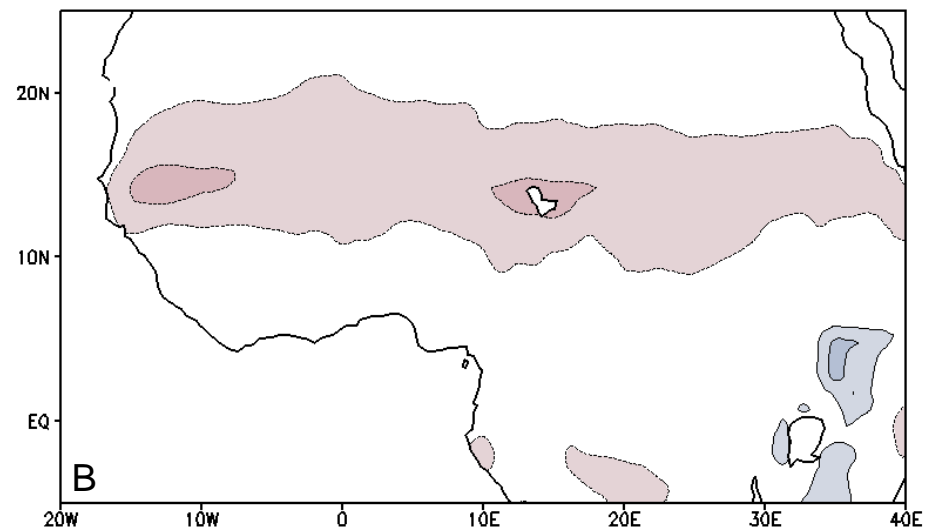
1170

1171   Figure 7. JJAS ensemble mean difference between Case 80SST and Case 50SST (mm day^{-1}) (a)

1172   vertical integrated moisture flux convergence (VIMFC) and (b) evapotranspiration

1173

1174   Figure 8. (a) Simulated VIMFC difference temporal evolution from Case 80SST – Case 50SST

1175   ensemble mean; (b) same as (a) but for Indian Ocean SST effect; (c) same as (a) but for Pacific

1176   Ocean SST effect; (d) simulated evapotranspiration evolution. Units: mm day^{-1}

1177

1178   Figure 9. Simulated temporal evolution of surface energy components differences between Case

1179   80SST and Case 50SST (a) total cloud cover; (b) downward short wave radiation; (c) upward short

1180   wave radiation; (d) downward long wave radiation; (e) upward long wave radiation; (f) surface net

1181   radiation; (g) sensible heat flux; (h) latent heat flux. Units: Total Cloud Cover: %; Others: W m^{-2}

1182

1183   Figure 10. Simulated temperature difference between Case 80SST and Case 50SST ensemble

1184   mean (a) evolution, (b) JJAS difference. Unit: °C

1185

1186   Figure 11. LULCC experimental design: (a) fraction changes of crop and pasture area between

1187   the 1990s and the 1950s (based on Hurtt data (2006); (b) ensemble mean albedo difference between

1188   Case LULCC and Case CTL; (c) same as (b) but for LAI; (d) dynamic vegetation model-simulated

1189   evolution of LAI anomaly over Sahel

1190

1191   Figure 12 (a) JJAS mean precipitation difference between Case LULCC and Case CTL; (b)

1192   temporal evolution of precipitation difference between Case LULCC and Case CTL; (c) same as

1193   (a) but for surface temperature; (d) same as (b) but for surface temperature. Units: Precipitation:

1194   mm day^{-1}; Temperature: °C.

1195

1196   Figure 13 (a) Simulated JJAS difference of 950 hPa wind vectors (m/s) and SLP (hPa) between

1197   Case LULCC and Case CTL; (b) latitude-height cross section of JJAS difference streamline (v, -

1198   100*w) averaged between 10°W and 10°E between case LULCC and case CTL

1199

1200   Figure 14. (a) JJAS ensemble mean difference of vertical integrated moisture flux convergence

1201   between Case LULCC and Case CTL; (b) same as (a) but for evaporation; (c) simulated VIMFC

1202   difference temporal evolution from Case LULCC – Case CTL; (d) same as (c) but for

1203   evapotranspiration. Units: mm day^{-1}

1204

Figure

Figure 1. (a, b) SST and precipitation SVD1 spatial patterns; (c) SVD PC1 time series during the 1950–2010 period; (d) WAMME SST forcing difference between 1980s and 1950s

Figure 2. JJAS mean observed and simulated precipitation (mm/day): (a) GTS climatology; (b) GTS precipitation difference between the 1980s and the 1950s; (c) Reanalysis I precipitation difference between the 1980s and the 1950s; (d)-(j) individual model simulated difference between Case 1980SST and Case 1950SST; (k) ensemble mean difference for global SST effect; (l)-(o) ensemble mean for each ocean basin effect. The corresponding climatology from observation and simulations for each model are displayed as contour lines in (b)-(k)

Figure 3. Observed and simulated precipitation temporal evolution (mm/day): (a) GTS climatology; (b) GTS precipitation difference between the 1980s and the 1950s; (c) Reanalysis I precipitation difference between the 1980s and the 1950s; (d)-(j) individual model simulated difference between Case 1980SST and Case 1950SST; (k) ensemble mean difference for global SST effect;(l)-(o) ensemble mean difference for each ocean basin effect. The corresponding climatology from observation and simulations for each model are displayed as contour lines in (b)–(k).

Figure 4. Taylor diagram for JJAS precipitation anomaly
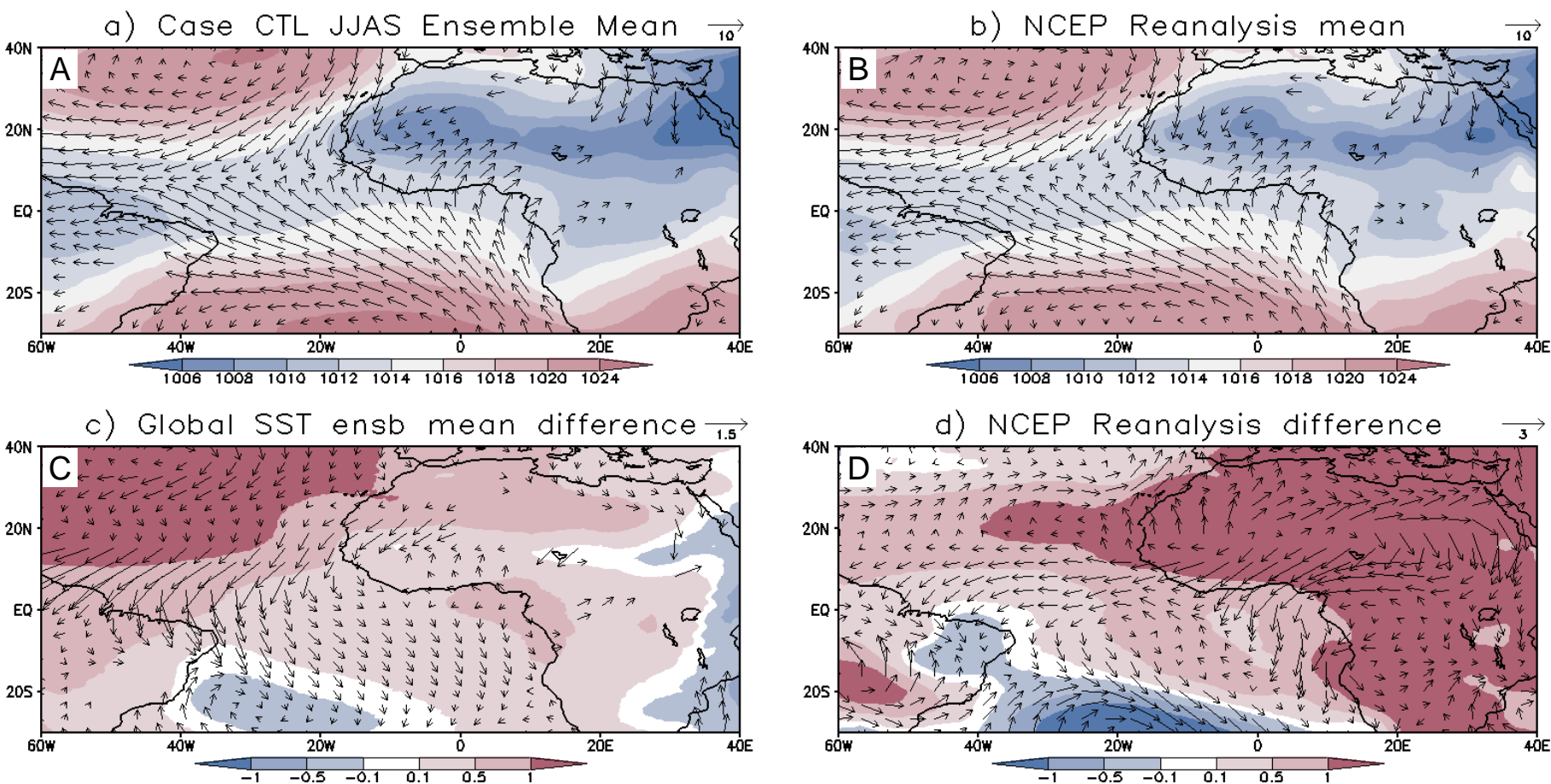
Figure 5. Simulated JJAS mean and anomalies of 950 hPa wind vectors (m/s) and SLP (hPa): (a) Case CTL ensemble mean; (b) NCEP Reanalysis climatology; (c) Case 80SST – Case 50SST ensemble mean; (d) NCEP Reanalysis difference between the 1980s and the 1950s

Figure 6. Latitude-height cross section of JJAS mean and anomaly streamline (v, -100*w) averaged between 10°W and 10°E: (a) Case CTL ensemble; (b) Case 80SST – Case 50SST ensemble mean; (c) NCEP reanalysis climatology; ((d) NCEP Reanalysis difference between the 1980s and the 1950s; (e) Indian Ocean SST effect; (f) Pacific Ocean SST effect. Note: The average of zonal wind or zonal wind differences are in shade (m s^{-1})
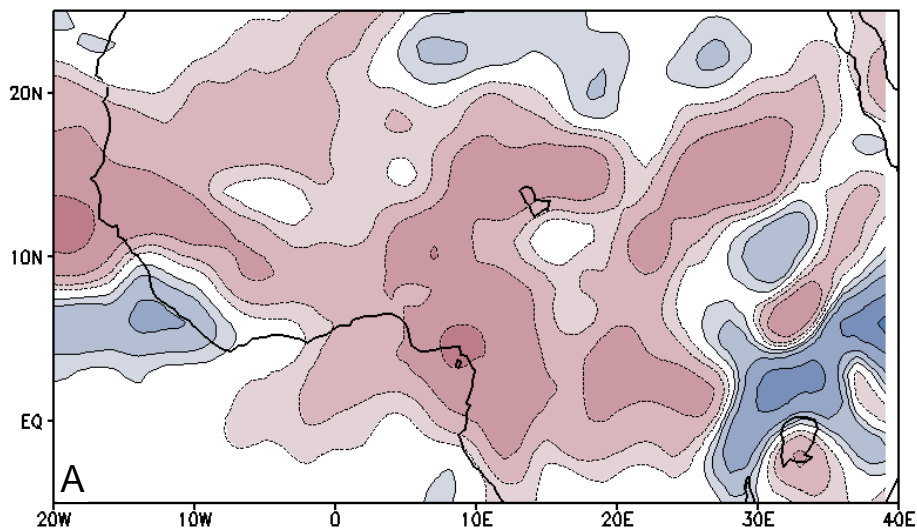
Figure 7. JJAS ensemble mean difference between Case 80SST and Case 50SST (mm/day) (a) vertical integrated moisture flux convergence (VIMFC) and (b) evapotranspiration
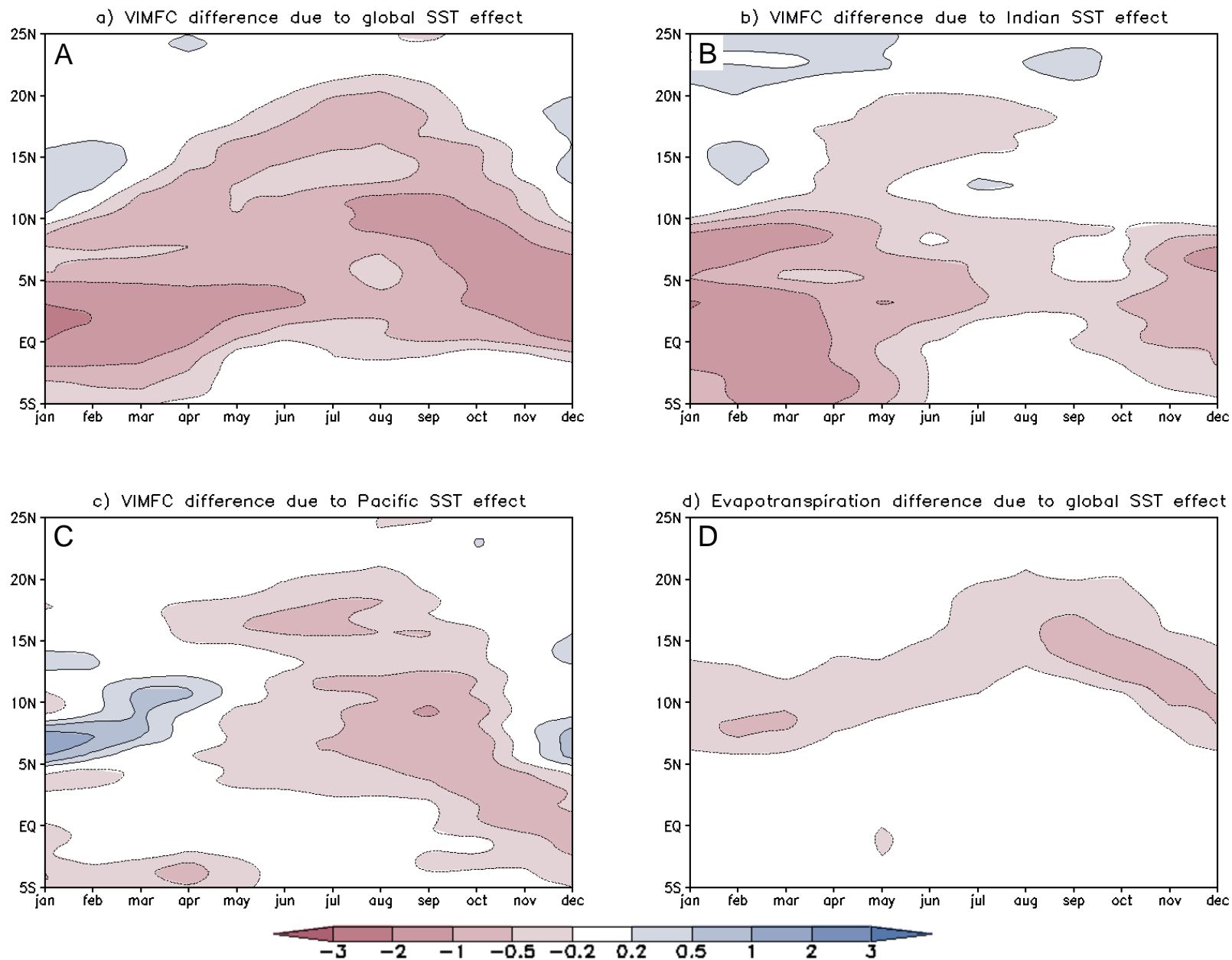
Figure 8. (a) Simulated VIMFC difference temporal evolution from Case 80SST – Case 50SST ensemble mean; (b) same as (a) but for Indian Ocean SST effect; (c) same as (a) but for Pacific Ocean SST effect; (d) simulated evapotranspiration evolution. Units: mm/day
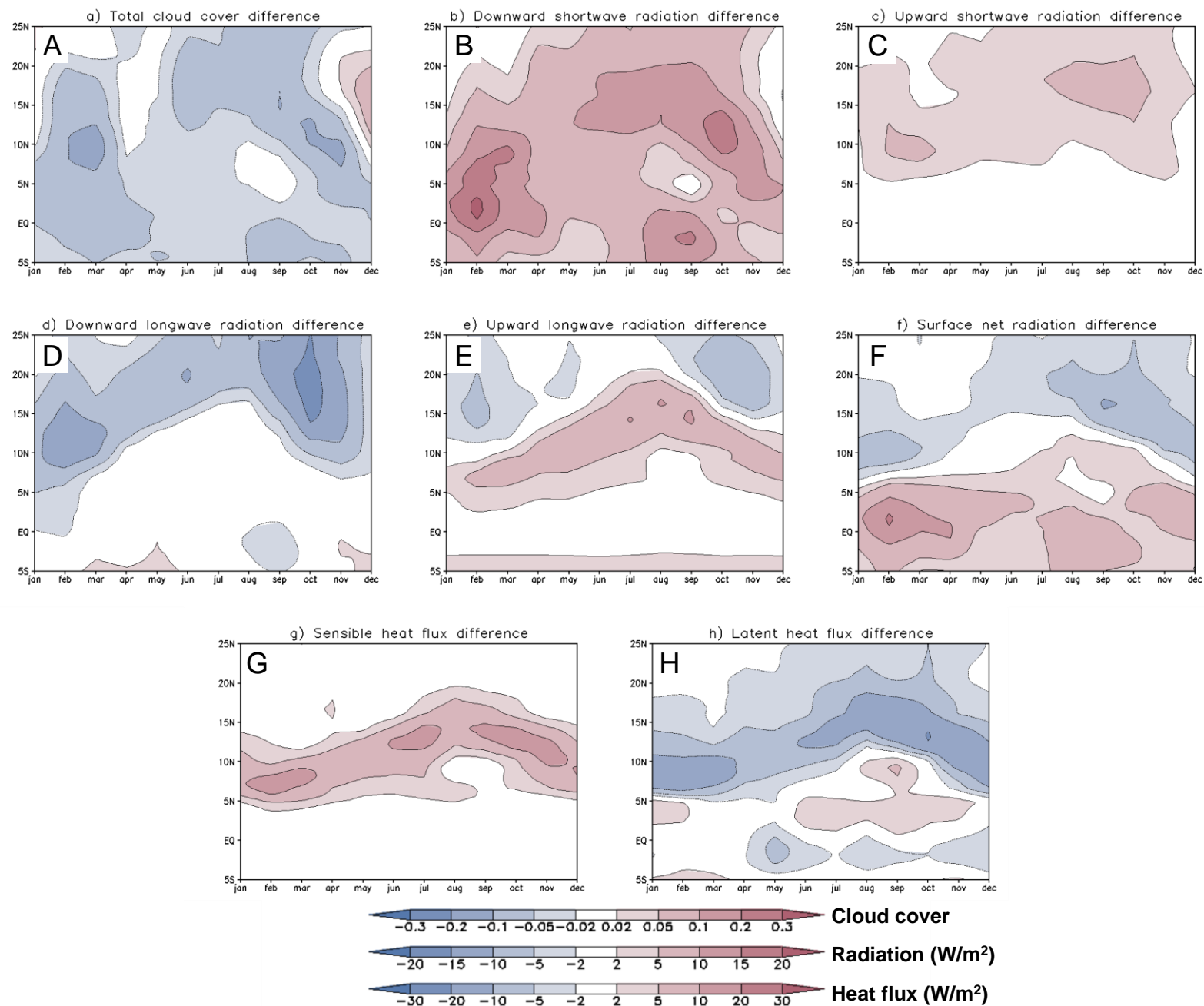
Figure 9. Simulated temporal evolution of surface energy components differences between Case 80SST and Case 50SST (a) total cloud cover; (b) downward short wave radiation; (c) upward short wave radiation; (d) downward long wave radiation; (e) upward long wave radiation; (f) surface net radiation; (g) sensible heat flux; (h) latent heat flux. Units: Total Cloud Cover: %; Others: W m^{-2}
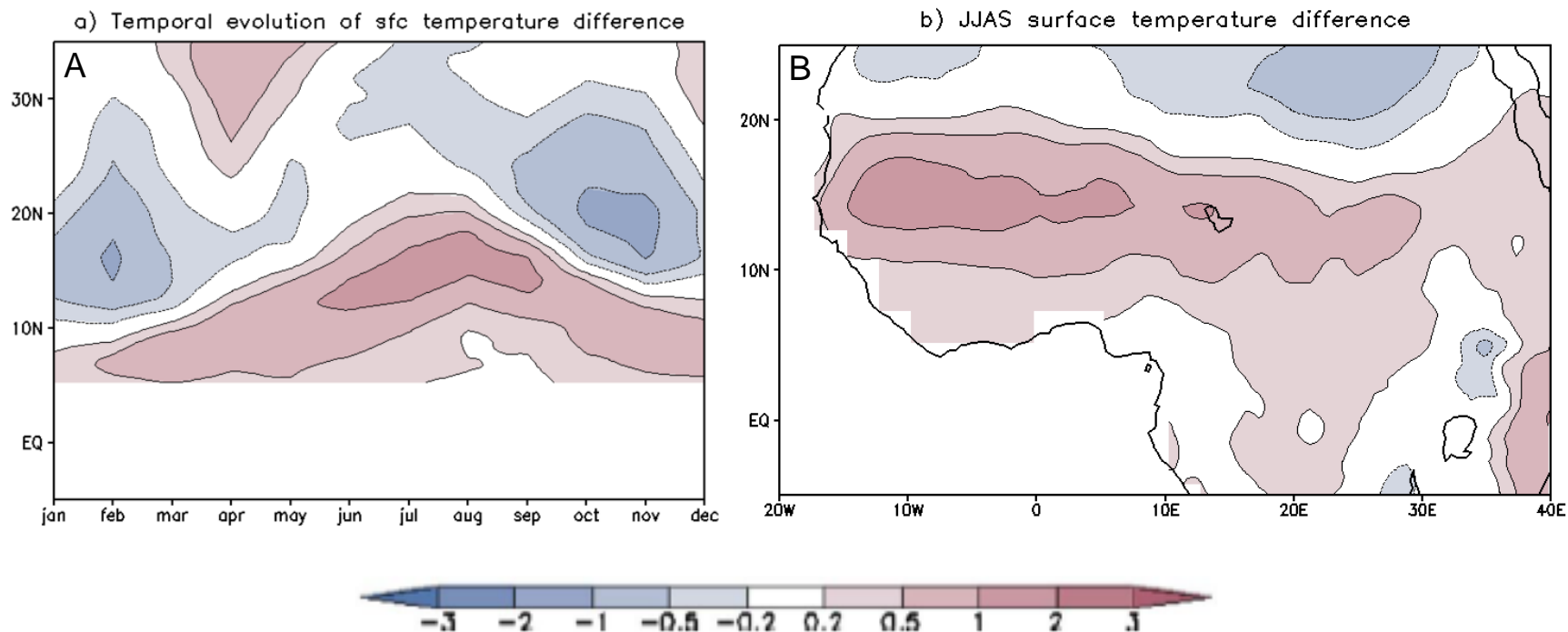
Figure 10. Simulated temperature difference between Case 80SST and Case 50SST ensemble mean (a) evolution, (b) JJAS difference. Unit: °C
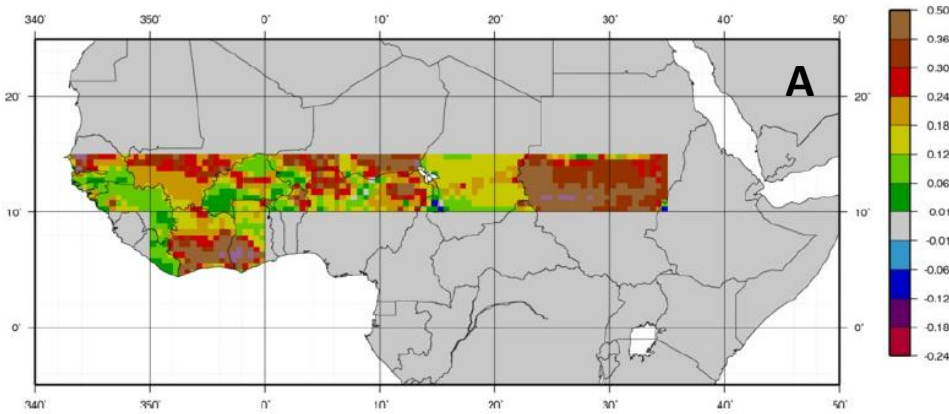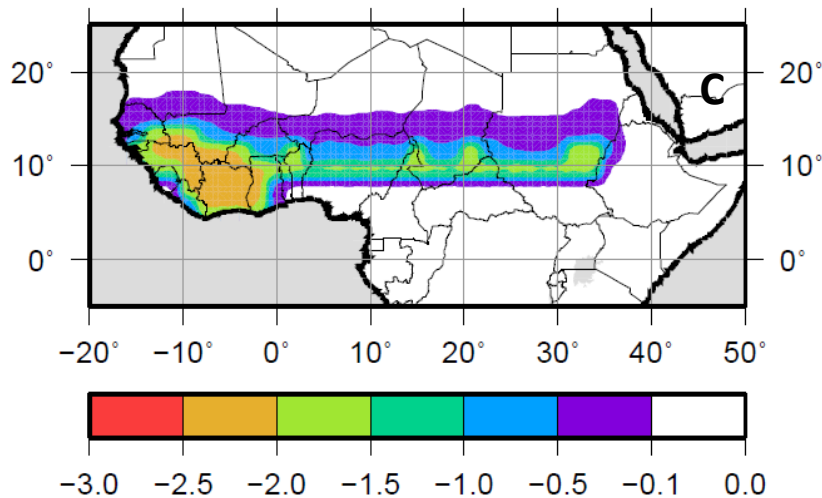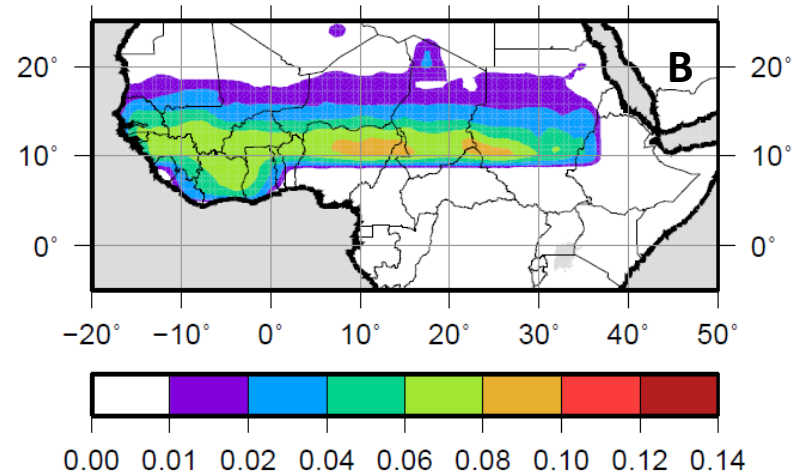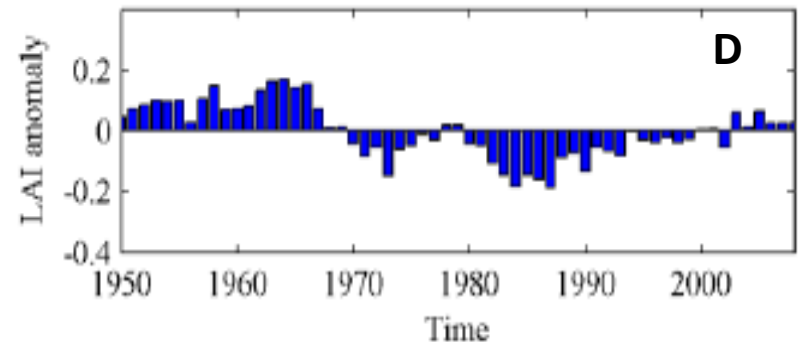
Figure 11. LULCC experimental design: (a) crop and pasture area changes between the 1990s and the 1950s (based on Hurtt data (2006); (b) ensemble mean albedo change between Case LULCC and Case CTL; (c.) same as (b) but for LAI; (d) dynamic vegetation model-simulated evolution of LAI anomaly over Sahel
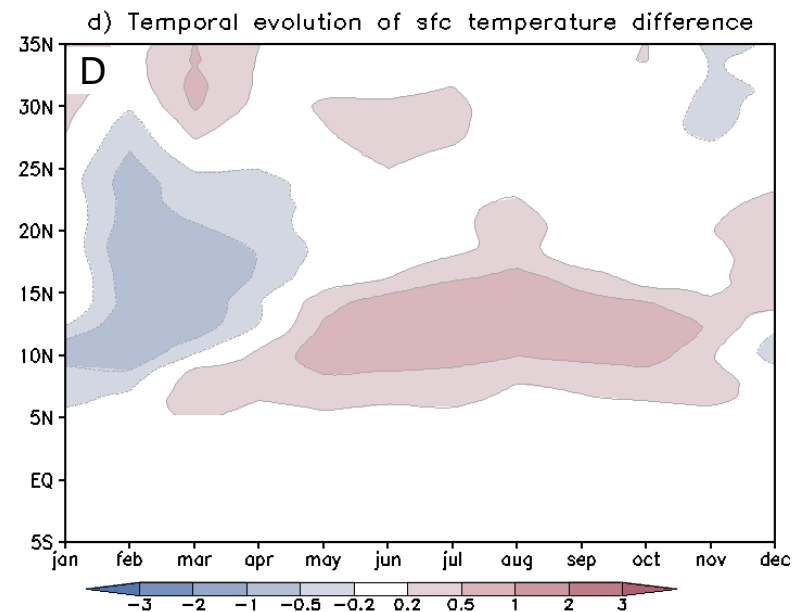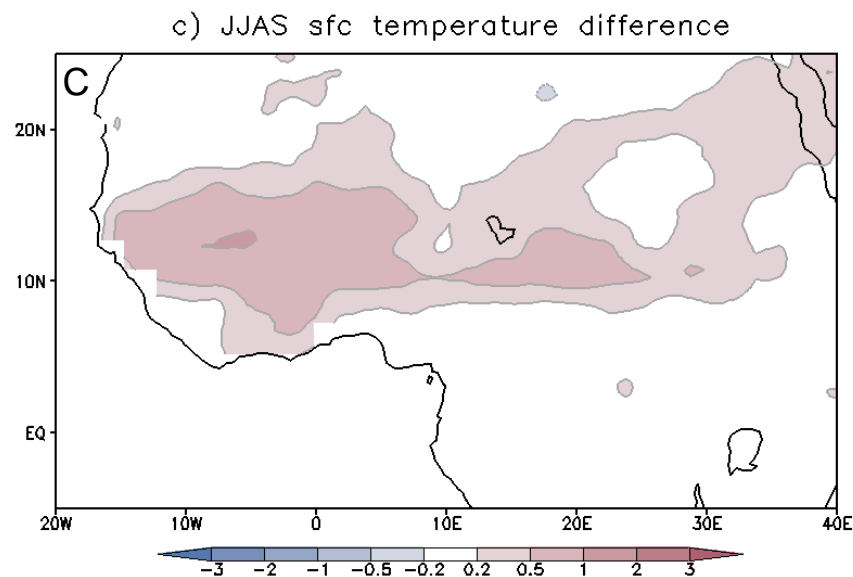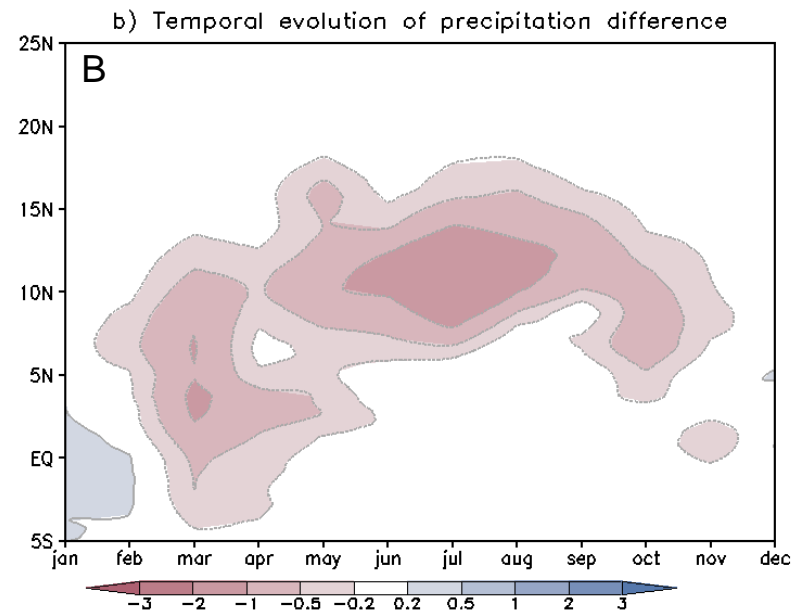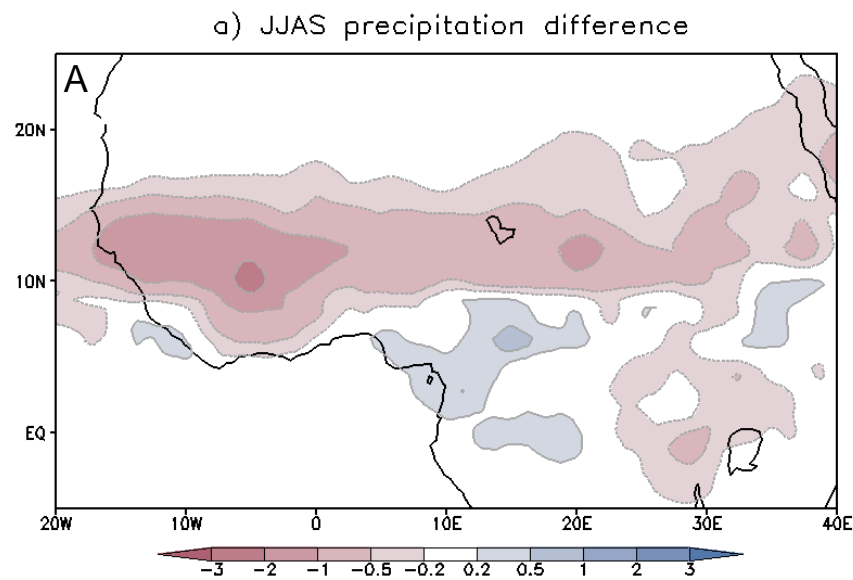
Figure 12 (a) JJAS mean precipitation difference between Case LULCC and Case CTL; (b) temporal evolution of precipitation difference between Case LULCC and Case CTL; (c) same as (a) but for surface temperature; (d) same as (b) but for surface temperature. Units: Precipitation: mm/day; Temperature: °C.
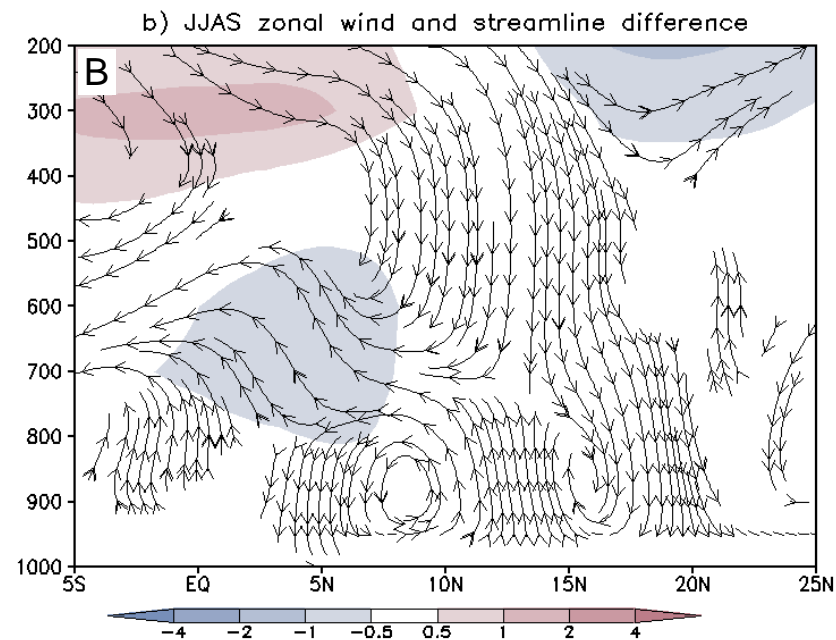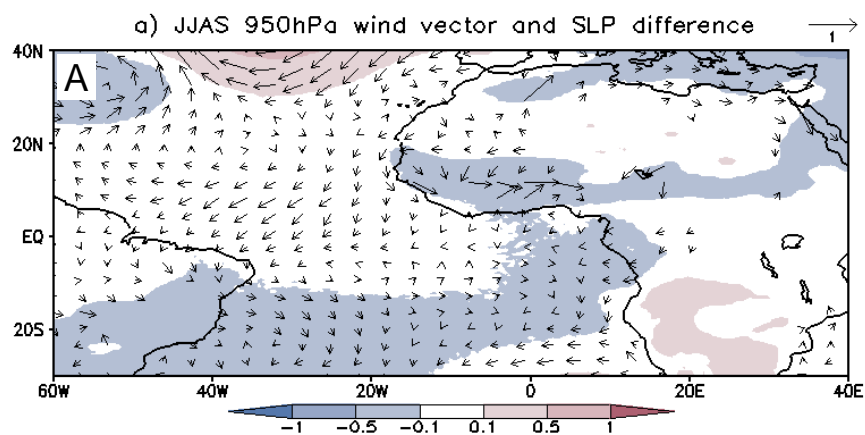
Figure 13 (a) Simulated JJAS difference of 950 hPa wind vectors (m/s) and SLP (hPa) between Case LULCC and Case CTL; (b) latitude-height cross section of JJAS difference streamline (v, -100*w) averaged between 10°W and 10°E between case LULCC and case CTL
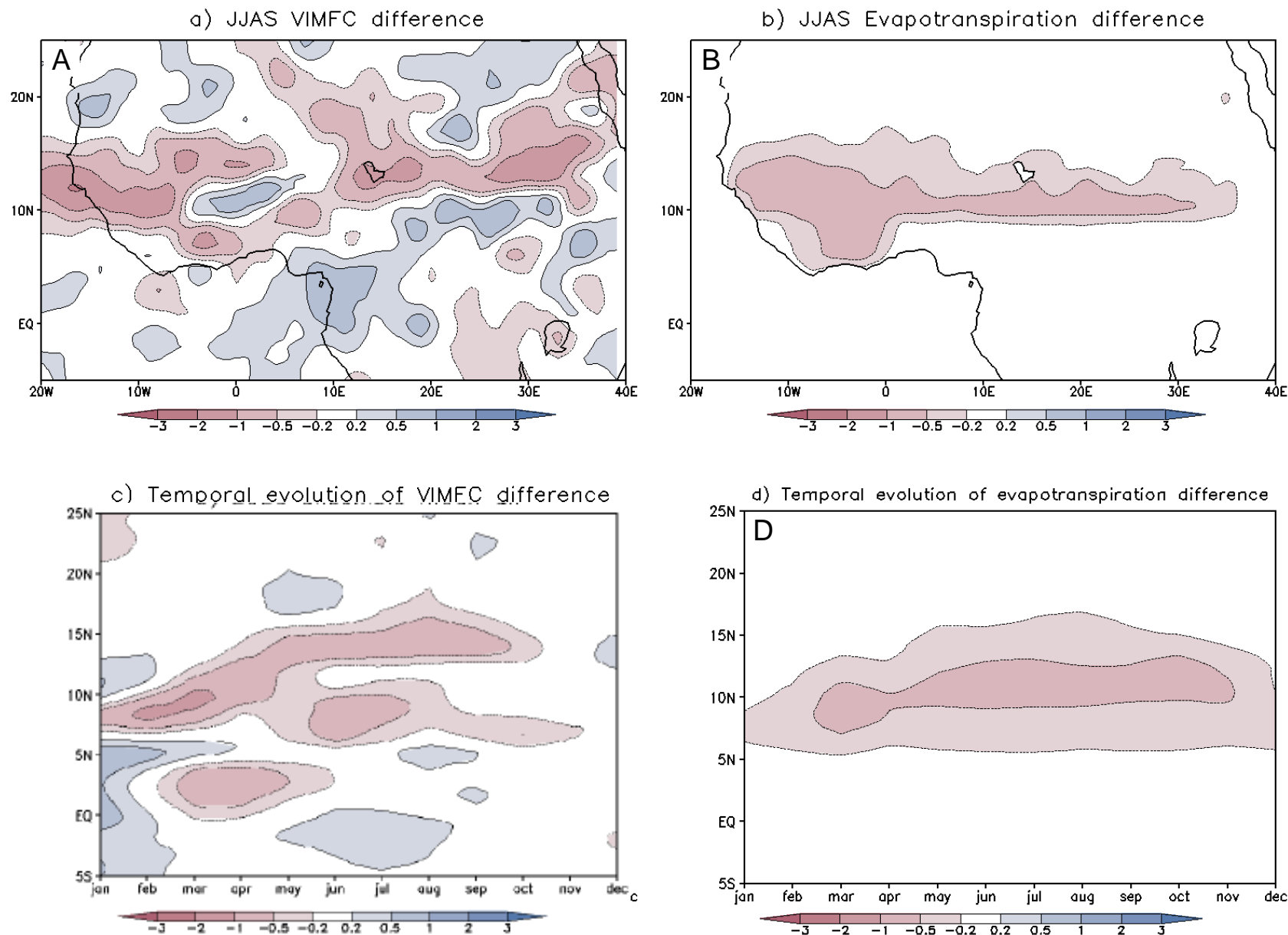
Figure 14. (a) JJAS ensemble mean difference of vertical integrated moisture flux convergence between Case LULCC and Case CTL; (b) same as (a) but for evaporation; (c) simulated VIMFC difference temporal evolution from Case LULCC – Case CTL; (d) same as (c) but for evapotranspiration. Units: mm/day

Appendix Figure A1. Comparison of JJAS precipitation difference between the 1980s and the 1950s from different observational data sets (mm/day)
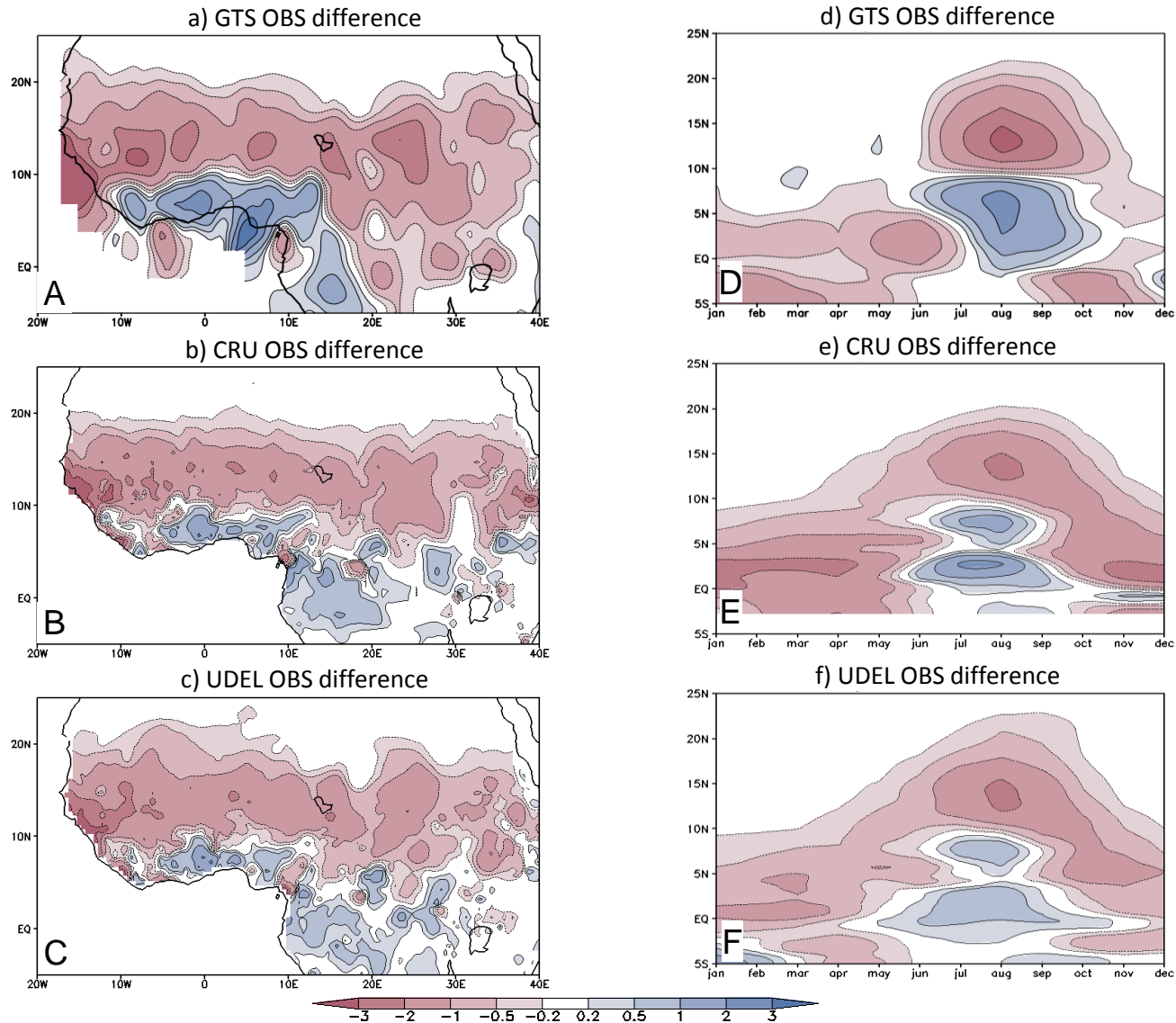
Appendix Figure A2. JJAS anomaly precipitation (mm/day) due to Atlantic SST anomaly
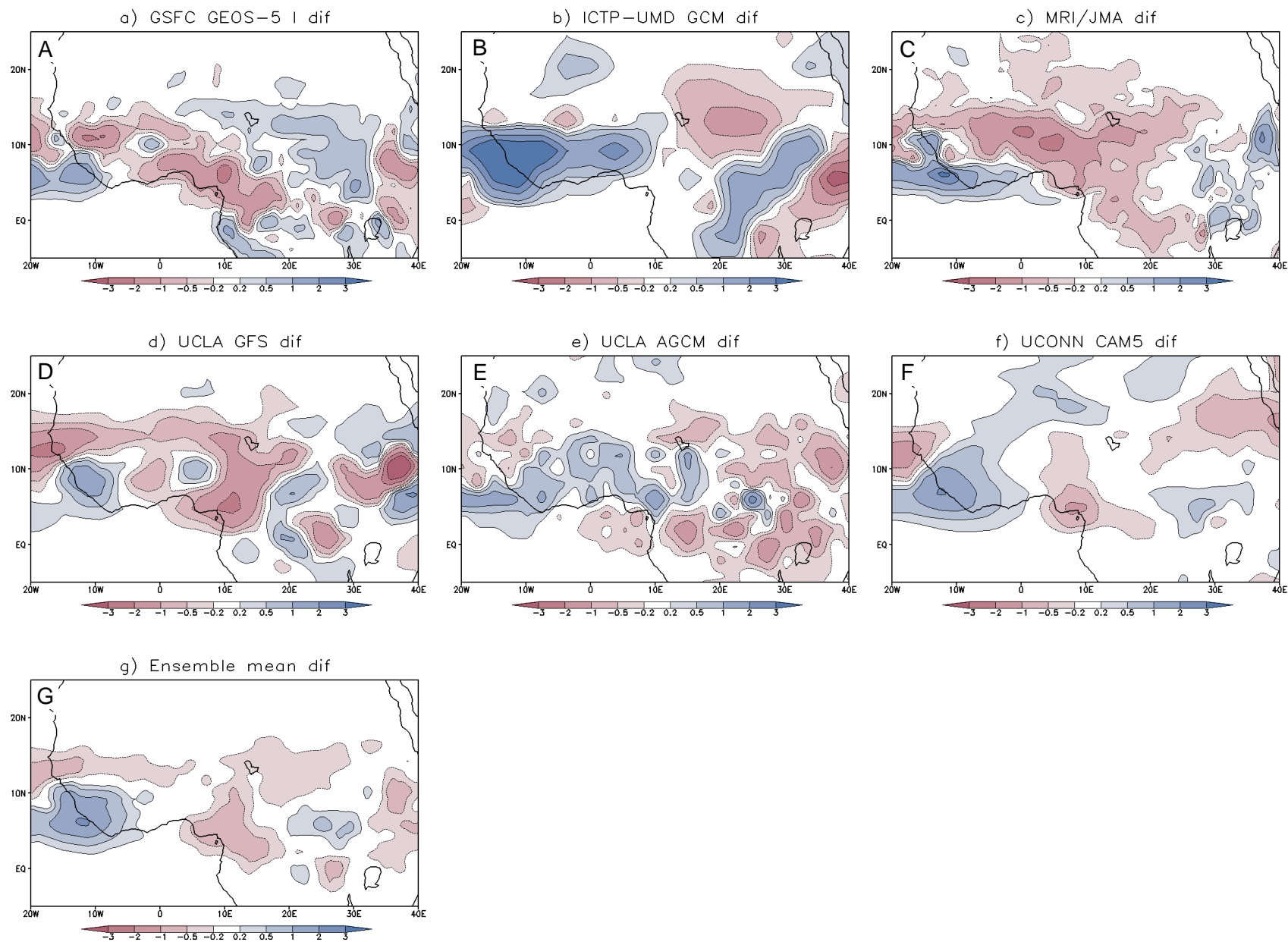
Appendix Figure A3. JJAS anomaly precipitation (mm/day) due to Mediterranean SST anomaly
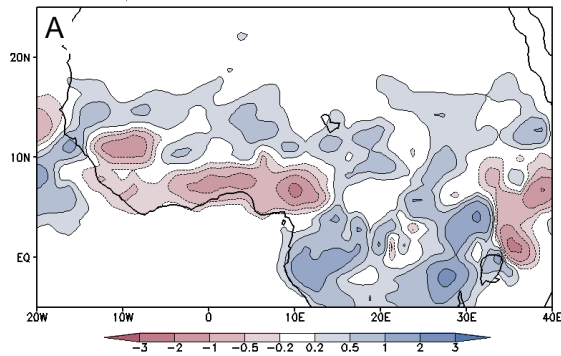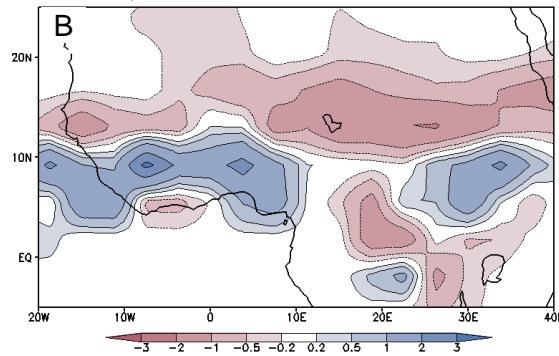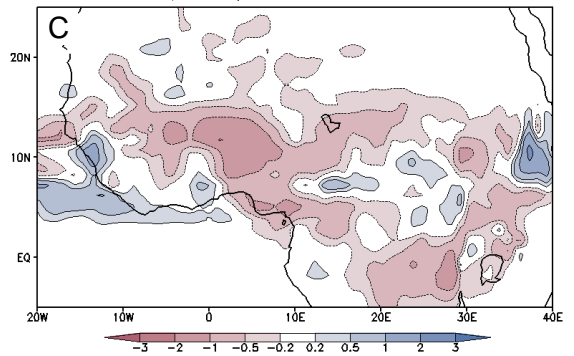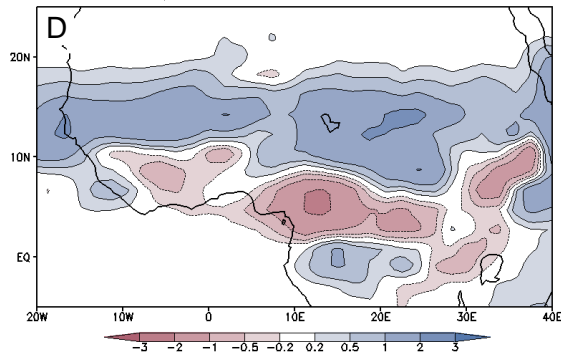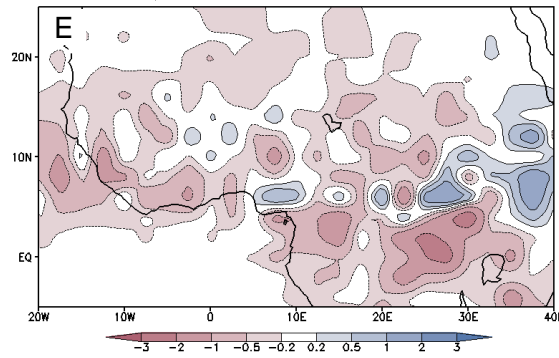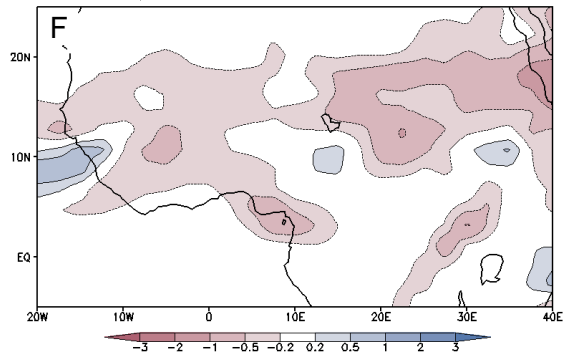
Table 1a. List of WAMME II GCMs

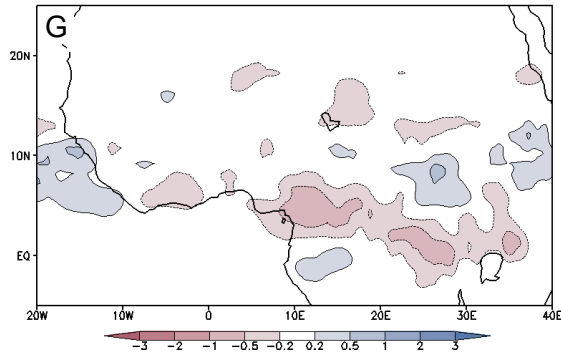| Model	Contact Person	Resolution	Rad. scheme	Conv. scheme	PBL/shallow cloud	Cloud	Surface	Aerosol/Dust
ICTP/UMD GCM (Kucharsk et al., 2013)	Fred Kucharsk, N. Zeng. E. Kalnay	T30L8 or T47L8	Molteni (2003)	Mass-flux (Molteni, 2003)	Molteni (2003)	Molteni (2003)	SL and-VEGAS (Zeng et al., 2000, 2003,2005)	
Japan MRI/JMA AGCM *(Mizuta et al., 2006)*	Masahiro Hosaka, A. Kitoh	TL959L60	Shibata and Uchiyana (1992); Shibata and Aoki (1989)	Prognostic Arakawa-Schubert (1974)	Stratoscumulus param. Slingo, (1987)	Smith (1999)	SiB with 4 soil layers, 3 snow layers (Sellers et al., 1996)	Sulfate aerosols, no dust
Modified NASA GMAO GEOS-5 (Molod et al., 2012)	K.-M. Lau K. M. Kim Y.-K. Kim S. Schubert	1° x 1.25° x L72 layers	Chou and Suarez (1999); Chou et al. (2001), with *parameterization modification*	Relaxed Arakawa Schubert (1974) with stochastic Tokioka parameter	Lock (2000) and Louis (1982)	Bacmeister et al. (2000)		Aerosol from GOCART model (Chin et al., 2002; Colarco et al., 2010)
NASA GMAO GEOS-5 (Molod et al., 2012)	Sarith, Mahanama, R. Koster	1° x 1.25° x L72 layers	Chou and Suarez, (1999); Chou et al. (2001)	Relaxed Arakawa Schubert (1974) with stochastic Tokioka parameter	Lock (2000) and Louis (1979)	Bacmeister et al. (2000)	Catchment model (Koster et al., 2000)	Aerosols from GOCART data
UCLA AGCM *(Mechoso et al., 2000)*	C. R. Mechoso, K. Schiro	2.5° x 2° x L17	Katayama (1972); Harshvardhan et al., (1987)	Arakawa and Schubert (1974); Lord et al. (1982)	Suarez et al. (1983)	Prognostic cloud water and ice (Kohler, 1999)	SSIB-1 (Xue et al., 1991)	No aerosol or GOCART Data
UCLA GFS GCM *(Kanamitsu et al., 2002, Xue et al., 2004b)*	Y. Xue, F. De Sales	T62L28	Chou (1992); Chou and Suarez (1999); Hou et al (1996, 2002)	Moorthi and Suarez (1992)	Hong and Pan (1996)	Slingo, 1987	SSIB-1 (Xue et al., 1991)	No aerosol or GOCART Data
Univ. of Connecticut CAM5 (Neale et al., 2012)	G. Wang	T63L26	RRTMG Iacono et al. (2008) and Mlawer et al. (1997)	Zhang & MaFarlane (1995); Richter & Rasch (2008); Raymond & Blyth (1992)	Bretherton & Park, (2009); Park & Bretherton (2009)	Gettelman et al. (2010)	CLM4.0 (Oleson et al., 2010)	Easter et al. (2004); Neale et al. (2012)
HadGEM2-A (HadGEM2 Model Deveopment Team, 2011)	R. Comer	1.25° x 1.875°x L38	Edwards and Slingo (1996); Cusack et al. (1999)	Gregory and Rowntree (1990); Grant and Brown (1999); Derbyshire (2011)	Lock et al. (2000); Brown and Grant (1997)	Smith et al. (1999). Wilson and Ballard (1999)	Cox et al. (1999); hydrology scheme (Clark & Gedney, 2008)	Bellouin et al. (2011); Collins et al. (2008); Woodward (2011)

Table 1b. List of WAMME II RCMs

Model	Contactp erson	Resolution	Rad. scheme	Conv. scheme	PBL/shallow cloud	Cloud	Surface	Aerosol / Dust
RegCM4.1 (with BATS)	Seidou Sanda Ibrah	50 km	CCM3 radiation (Kiel et al., 1996)	Grell (1994)	Holtslag et al. (1990)	Grell (1994)	BATS, (*Dickinson et al.*, 1986)	Solmon et al. (2006) Zakey et al. (2006)
UCLA WRF	Y. Xue F. De Sales	50x50 km, 38 levels	Fels and Schwartzkopf, (1975)	Betts-Miller-Janjic (Janic, 1990)	Mellor-Yamada 2.5 (Mellor & Yamada, 1982; Janic, 1996)	Zhao and Carr (1997)	SSIB-3 (Xue et al., 1991; Sun and Xue, 2001)	
WRF 3.3 (CAM physics) (Skamarock et al., 2008)	Samson Hagos	25 km	RRTM	Zhang and McFarlane (1995)	UW shallow (Bretherton and Park 2004)	Morrison-Gettelman (CAM5)	NOAH (Chen, & Dudhia, 2001; SSiB (Xue et al., 1991; Sun and Xue, 2001), Pleim-Xiu (Pleim & Xiy, 2003)	
RegCM4.1 (with CLM4) (Wang et al., 2015a)	G. Wang	50 km	CCM3 radiation (Kiel et al., 1996)	Emanuel (1991)	Holtslag et al. (1990)	Emanuel (1991) and Pal et al. (2000)	CLM4 (Oleson et al., 2010)	(not activated) Solmon et al. (2006) Zakey et al. (2006)

Note: References cited in Table 1 can be found at http://www.wamme.geog.ucla.edu/LOCAL/ref_gcm_wamme.pdf

Table 2. Observed and Model-Simulated Variable Differences over the Reference Area[1,2]

	Names	Precipitation (P)		Ts	Evapotranspiration (E)		VIMFC	
		Difference[3] (ΔP)	Relative Difference[4]		Difference[3] (ΔE)	ΔE/ΔP	Difference[3] (ΔVIMFC)	ΔVIMFC/ΔP
Observation and Reanalysis	GTS	-1.41	-44%					
	UDEL	-1.21	-35%	0.96				
	CRU	-1.11	-33%	1.11				
	Reanalysis I	-1.43	-51%	0.85	-0.29	20%	-1.14	80%
Models	GSFC GEOS-5	-0.18	-7%	0.29	-0.09	47%	-0.10	53%
	ICTP-UMD	-0.79	-20%	0.62	-0.26	33%	-0.53	67%
	MRI/JMA	-0.93	-31%	0.8	-0.28	30%	-0.65	70%
	UCLA GFS	-1.39	-53%	1.17	-0.46	33%	-0.93	67%
	UCLA AGCM	-1.08	-35%	1.16	-0.54	50%	-0.54	50%
	UCONN CAM5	-0.77	-20%	0.67	-0.17	22%	-0.60	78%
	Ensemble mean	-0.86	-27%	0.78	-0.30	35%	-0.56	65%

Note: 1). Units: precipitation: mm day^{-1}; surface temperature: K; Evapotranspiration: mm day^{-1}; Vertical Integrated Moisture Flux Convergence (VIMFC): mm day^{-1}.
2). Reference Area: 10°N to 20°N and 10°W to 10°E.
3). Differences for observation and Reanalysis are based on the differences between the 1980s and the 1950s. Simulated differences are based on 1980s SST and 1950s SST. The GSFC GEOS-5 results are based on the average of GEOS-5 I and GEOS-5 II.
4). Precipitation Relative Difference: for observational data: observed difference / observational climatology; for simulations: simulated difference by one model / this model's climatology.

Table 3. Observed and Simulated Differences over the Reference Area due to Different Forcings[1,2]

| Scenarios | Precipitation (P) | | Ts | Evapotranspiration (E) | | VIMFC | |
	Difference[3] (ΔP)	Relative Difference to Observation[4]		Difference (ΔE)	ΔE/ΔP	Difference (ΔVIMFC)	ΔVIMFC/ΔP
GTS	-1.41		0.96[6]				
Global SST	-0.86	61%	0.78	-0.30	35%	-0.56	65%
India SST	-0.32	23%	0.34	-0.13	41%	-0.19	59%
Pacific SST	-0.50	35%	0.41	-0.12	24%	-0.38	76%
LULCC[5]	-0.60	43%	0.50	-0.32	54%	-0.23	46%

Notes: 1). Units: precipitation: mm day^{-1}; surface temperature: K; Evapotranspiration: mm day^{-1}; Vertical Integrated Moisture Flux Convergence (VIMFC): mm day^{-1}.

2). Reference Area: 10°N to 20°N and 10°W to 10°E.

3). Differences for observation and Reanalysis are based on the differences between the 1980s and the 1950s. Simulated differences are based on 1980s SST and 1950s SST. The GSFC GEOS-5 results are based on the average of GEOS-5 I and GEOS-5 II.

4). Precipitation Relative Difference for simulations: simulated difference between Case 80SST and Case 50SST / observed difference between the 1980s and the 1950s.

5). Land use land cover changes (LULCC) are based on the degraded vegetation map and control vegetation map.

6). Data are based on UDEL observational data

Table 4. Surface Energy Balance Differences over the Reference Area

	CLD	SWD	SWU	LWD	LWU	Net Rad	LH	SH	Temperature
Observation									0.96
Reanalysis I	-0.13	26.24	6.95	-4.93	5.71	8.65	-8.40	17.09	0.85
Global SST	-0.07	10.99	4.00	-3.37	6.22	-2.60	-8.61	5.70	0.78
LULCC	-0.03	6.91	10.87	-1.68	3.61	-9.25	-9.32	-0.23	0.50

Note: 1). Units: surface temperature: K; All other variables: w m^{-2}.

2). Reference Area: 10°N to 20°N and 10°W to 10°E.

3). Observation and Reanalysis I are based on the differences between the 1980s and the 1950s

4). Global SST is based on Case SST80 minus Case SST50

5). LULCC is based on the difference between Case LULCC and Case CTL.

6). Abbreviations: CLD: Total cloud cover; SWD/SWU: Short wave radiation down/up; LWD/LWU: long wave radiation down/up; Net Rad: net radiation; LH: latent heat flux; SH: Sensible heat flux.

Click here to access/download
Electronic Supplementary Material
Electronic Supplements_II_final.docx

Click here to access/download
Electronic Supplementary Material
Figures for Electronic Supplement_II_final.pptx